

Poroelastic Benchmarking of a Finite Element Multiphysics Code

Robert Lewis Walker¹ and Matthew Knepley¹

¹University at Buffalo

August 30, 2023

1

Multiphysics Modeling in PyLith: Poroelasticity

2

Robert L. Walker¹, Matthew G. Knepley¹, Brad T. Aagaard², Charles A.

3

Williams³

4

¹University at Buffalo

5

²U.S. Geological Survey

6

³GNS Science

Corresponding author: Robert L. Walker, rainbowseismic@gmail.com

Abstract

PyLith, a community, open-source code (<https://geodynamics.org/resources/pylith/>) for modeling quasi-static and dynamic crustal deformation with an emphasis on earthquake faulting, has recently been updated with a flexible multiphysics implementation. We demonstrate the versatility of the multiphysics implementation by extending the code to model fully coupled continuum poromechanics. We verify the newly incorporated physics using standard benchmarks for a porous medium saturated with a slightly compressible fluid. The benchmarks include the one-dimensional consolidation problem as outlined by Terzaghi, Mandel's problem for the two-dimensional case, and Cryer's problem for the three-dimensional case. All three benchmarks have been added to the PyLith continuous integration test suite. We compare the closed form analytical solution for each benchmark against solutions generated by our updated code, and lastly, demonstrate that the poroelastic material formulation may be used alongside the existing fault implementation in PyLith.

Keywords

Permeability and porosity; Mechanics, theory, and modelling; Rheology: crust and lithosphere

1 Introduction

Observations of the interaction between interstitial fluids and solid earth mechanics have a long history. Pliny the Elder described hydrological changes following ancient earthquakes (Bostock & Riley, 2011), and Leonardo da Vinci formalized the analogy of Earth as a living body (da Vinci, 2019). Interaction between pore fluid and porous media is also key to petroleum recovery and drives the field of subsurface hydrology. Poroelastic coupling between solid and fluid material phases plays an important role in geodynamics problems, including the deformation mechanisms involved in faulting, earthquake triggering, and magma movement. Physical interaction between a solid matrix and the fluid contained within its pore spaces occurs through two complementary mechanisms coupling the material phases. An increase in pore fluid pressure tends to cause the solid to dilate, whereas compression of the solid will result in an increase in pore fluid pressure, potentially driving fluid flow. When fluid diffuses through solid material in response to compression, the solid will deform as the pore fluid pressure falls (Cheng, 2016). These coupled processes result in deformation that is controlled by fluid flow through the porous domain. We model this elastic interaction in PyLith, augmenting our existing viscoelastic and elastoplastic models of crustal deformation.

41 PyLith (Aagaard et al., 2007, 2013; Aagaard, Knepley, Williams, & Walker, 2022;
42 Aagaard et al., 2023), is portable, scalable community software for simulation of crustal
43 deformation across spatial scales ranging from meters to hundreds of kilometers and tem-
44 poral scales ranging from milliseconds to thousands of years. Its primary applications
45 are quasi-static and dynamic modeling of earthquake faulting. The original design of PyLith
46 included a displacement solution field and a Lagrange finite element with linear basis func-
47 tions. The latest version of PyLith (Aagaard, Knepley, & Williams, 2022b) involves a
48 complete redesign of the finite-element formulation of the governing equations, using the
49 discretization and finite element assembly tools from the PETSc libraries (Balay et al.,
50 2023b). PyLith uses the support for parallel unstructured meshes (Knepley & Karpeev,
51 2009; Lange et al., 2016; Knepley et al., 2017; Wallwork et al., 2022) including parallel
52 loading, partitioning and redistribution, finite-element function representation with local-
53 to-global maps, and assembly of finite-element functions and operators from weak forms.
54 This allows PyLith to support implementation of different governing equations and so-
55 lutions containing multiple fields (e.g., displacement, velocity, fluid pressure, and tem-
56 perature).

57 We leverage this newly-implemented multiphysics framework to add poroelastic mod-
58 eling abilities in PyLith, allowing us to model these coupled geomechanical problems.
59 We create coupled poroelastic simulations, representing both the time-dependent fluid
60 flow as well as the associated elastic response.

61 **1.1 Observations of Poroelastic Deformation**

62 Poroelastic deformation arises in a variety of contexts. We highlight three categories
63 of observations that we want to model using the poroelasticity implementation in PyLith:
64 subsidence, post-seismic deformation, and induced seismicity.

65 **1.1.1 Subsidence**

66 Subsurface fluid withdrawal decreases *in situ* fluid pore pressure and decreases the
67 effective stress. This reduces resistance to compaction and produces subsidence. It has
68 been the subject of study since at least the nineteenth century (Poland & Davis, 1969).
69 Early recorded subsidence examples tended to be driven by groundwater extraction (Gurevich
70 & Chilingarian, 1995). Ground subsidence resulting from oil production was noted as
71 early as 1918 (Pratt & Johnson, 1926). An example of subsidence occurred at the Wilm-
72 ington, California, oil field, where a combination of heavy oil extracted using pressure
73 depletion and shallow reservoirs produced a vertical settlement of 8 meters (Poland &
74 Davis, 1969). The settlement was successfully mitigated through repressurization. The

75 subsidence may have also triggered local seismicity (Hough & Bilham, 2018; Hough &
76 Page, 2016).

77 ***1.1.2 Postseismic Deformation***

78 Poroelastic rebound can be one of the primary mechanisms driving postseismic de-
79 formation. In modeling the postseismic deformation of the 1992 M7.3 Landers, Califor-
80 nia, earthquake, Peltzer et al. (1998) found it was important to discriminate between sev-
81 eral possible deformation mechanisms, including afterslip, poroelastic rebound, and vis-
82 coelastic relaxation. They proposed poroelastic rebound associated with pore fluid flow
83 in the shallow crust to explain discrepancies between observations from space-based syn-
84 thetic aperture radar and the vertical displacement expected at distances of kilometers
85 from the fault for elastic modeling of horizontal slip occurring on a buried dislocation
86 in a Poisson's material. They favored this explanation over the alternative model of vis-
87 coelastic relaxation. The observed decay time of postseismic uplift fit the characteris-
88 tic time describing earthquake associated poroelastic rebound in the upper crust iden-
89 tified in previous studies (Muir-Wood & King, 1993; Nur & Booker, 1972).

90 ***1.1.3 Induced Seismicity***

91 Along with the early 21st century boom in North American tight shale production
92 came a corresponding rise in seismicity (Ellsworth, 2013). Many induced earthquakes
93 have been attributed to the process of hydraulic fracturing (Skoumal et al., 2015). In
94 the traditionally accepted model of injection-induced seismicity, pore pressure changes
95 result in a corresponding reduction of effective normal stress on critically stressed frac-
96 tures and faults. This was first outlined by the case of the triggered earthquakes at the
97 Rocky Mountain Arsenal, near Denver, Colorado (Healy et al., 1968), and later confirmed
98 by the experiment in earthquake control at the Rangely Oil Field in Rio Blanco county,
99 Colorado (Raleigh et al., 1976). The traditional view considered only the area subject
100 to pore pressure diffusion as at risk for triggered seismicity, thus permitting modeling
101 based on fluid diffusivity alone (Seeber et al., 2004; Stein, 1999). Pore pressure diffusion
102 alone does not account for all observed behavior. Documented earthquakes ascribed as
103 induced frequently occur in the crystalline basement well below the sedimentary layer
104 targeted for injection (Zhang et al., 2013). Similarly, seismicity often displays an erratic
105 spatial pattern when compared to the corresponding fluid injection. Clusters of observed
106 seismicity may occur well ahead of expected pressure fronts. Some of this may be ex-
107 plained by faults periodically acting as highly permeable channels such as in the "fault-
108 valving" hypothesis (Sibson, 1990), poroelastic stress transfer (Segall, n.d.) and aseis-

109 mic deformation can also play roles (Barros et al., 2019). Elastic stress resulting from
 110 coupling of pressure and stress is expected to extend to distances greater than pore pres-
 111 sure alone (Goebel et al., 2017; Segall & Lu, 2015). Fluid injection causes both a change
 112 in pore fluid pressure, resulting in a change in effective normal stress for nearby faults,
 113 as well as poroelasticity-induced stress changes in the porous matrix material. A fully
 114 coupled poroelastic model in conjunction with an earthquake production rate law could
 115 be used to help explain elevated seismicity rates near fluid injection sites.

116 1.2 Coupled Modeling

Hydrology and petroleum engineering disciplines have a long history of fluid mod-
 eling. When applied to the production of hydrocarbons, this has been referred to as reser-
 voir simulation and provides a basis for optimizing extraction. Traditionally, reservoir
 simulation focused on the numerical approximation of conservation of fluid mass and mo-
 mentum via Darcy’s Law. Engineers tasked with optimizing hydrocarbon production his-
 torically addressed rock mechanic issues, “only of dire necessity and then with little en-
 thusiasm” (Median, 1994). Much has changed since that quote was published. As inter-
 est shifted to more complex formations and horizontal drilling has become widespread
 geomechanics has become a central concern. Hydrocarbon reservoir simulation began with
 an expansion from analytical solutions of the fluid diffusion equation to gridded, numer-
 ical approximations of the same fluid flow representation (Odeh, 1982). This permitted
 treatment of more complicated domains (Craft et al., 1991). However, the focus was still
 firmly on fluid flow, especially multiphase flow. A simple form of reservoir compaction
 uses a time-invariant compressibility variable, c_R to update porosity through the rela-
 tion

$$\phi = \phi_0 (1 + c_R (p - p_0)). \quad (1)$$

117 Permeability may also be updated in this fashion through an empirical relation such
 118 as the Kozeny-Carmen equation (Carman, 1997). In numerical modeling the term “cou-
 119 pling” refers to combining multiple physical processes into a single model to determine
 120 a consistent solution. For the case of the coupling between fluid flow and mechanical stress,
 121 different levels of coupling have been described by many authors (R. Dean et al., 2003;
 122 Tran et al., 2004; Samier et al., 2006; R. H. Dean et al., 2006). We will assume the stan-
 123 dard practice of the hydrocarbon reservoir simulation community that the primary vari-
 124 able of interest is reservoir pore pressure. We outline the level of coupling ordered from
 125 least comprehensive to most comprehensive:

- 126 1. An **uncoupled or decoupled** system, where only one component is solved
127 for, and the other is incorporated by means of a coefficient (rock compressibility
128 for fluid diffusion, effective stress for mechanics). This is the traditional approach
129 taken in reservoir simulation.
- 130 2. In a **loosely or explicitly coupled** system the value for pore pressure is com-
131 puted, taking into account a known value for displacement. The resultant value
132 for pore pressure is then given to the geomechanics implementation in order to com-
133 pute the displacement. The coupling terms are calculated explicitly and lag one
134 step behind. In the simplest implementation of this method, known as a **one way**
135 **coupled** system, solutions for the primary variable of interest (in this example,
136 pore pressure) are fed into the mechanics problem (for example, geomechanics)
137 without feedback to the flow problem.
- 138 3. An **iteratively coupled** system is one where the equations for flow and stress are
139 solved separately, and the process repeated until the unknowns for stress and fluid
140 flow each converge. This approach (Jha & Juanes, 2014, 2007; Kim et al., 2011a)
141 offers the benefit of using separate codes for the flow and solid mechanics prob-
142 lems with relatively minor additional effort, and using different domains for dif-
143 ferent solution fields. Iterative coupling tends to be limited to first-order conver-
144 gence rates for the nonlinear iterations (R. H. Dean et al., 2006). Also, using too
145 large of a convergence tolerance can introduce spurious solutions (Ropp & Sha-
146 did, 2009; Béreux, 1996).
- 147 4. In a **fully coupled**, or fully implicit, approach all equations are solved simulta-
148 neously over the same domain. When solved implicitly with proper boundary and
149 initial conditions, this approach can yield unconditional stability and convergence
150 (Kim et al., 2011a, 2011b).

151 Coupling becomes crucial when the flow and deformation have a first-order effect
152 on each other (Dusseault, 2008; Rothenburg & Bathurst, 1989). The iterative approach
153 has traditionally been preferred due to the potentially high cost of solving the coupled
154 nonlinear equations. However, scalable preconditioners for the fully-coupled poroelas-
155 tic problem (Piersanti et al., 2021) and high performance implementations such as in the
156 MOOSE Framework (Gaston et al., 2009; Lindsay et al., 2022) have demonstrated that
157 a fully coupled approach can be both performant and flexible. Along with MOOSE it-
158 self, applications built off of MOOSE have taken advantage of the modular nature of the
159 code to produce fully coupled finite element multiphysics. GOLEM presented a fully cou-
160 pled, fully implicit thermo-hydro-mechanical model that, like PyLith, modeled faults as
161 one dimension lower than the surrounding domain (Cacace & Jacquy, 2017). FALCON

162 featured a second-order, hybrid continuous/discontinuous Galerkin finite-element method
 163 for thermo-hydro-mechanical (THM) problems (Xia et al., 2017; Podgorney et al., 2021).
 164 GOLEM has also been used to model laboratory faulting experiments using rate and state
 165 friction (Hutka et al., 2023), as well as stress changes in geothermal reservoirs (Cacace
 166 et al., 2021). Another package, OpenGeoSys, focused on thermo-hydro-mechanical-chemical
 167 (THMC) processes in porous and fractured media (Naumov et al., 2022).

168 Another example of a cOlav Møynerrcommunity code that has grown to incorporate
 169 coupled poroelasticity is the MATLAB Reservoir Simulation Toolbox (MRST) (Krogstad
 170 et al., 2015). This code took the opposite approach from PyLith, originating as a fluid
 171 flow simulator (Lie, 2019) and treating faults as part of the larger domain. In line with
 172 the sandbox nature of MRST, both iterative and fully coupled approaches are available,
 173 as well as the option of a finite volume representation of poromechanics (Knut-Andreas Lie,
 174 2021).

175 A plethora of custom implementations for poroelastic models exist, but we high-
 176 light generic, multiphysics implementations that allow users to easily change the domain,
 177 boundary and initial conditions, rheology, and formulation to suit their particular needs.
 178 Mardal et al. (2021) discretize poroelasticity using mixed finite elements in FEniCS (Logg
 179 et al., 2012, 2011) and show that it is not necessary to have a Darcy-stable pairing to
 180 have a stable formulation. Using both FEniCS and Firedrake (Rathgeber et al., 2017;
 181 Ham & Team, 2022), McCormack et al. (2020) model postseismic deformation and de-
 182 termine the contribution from poroelasticity. Wang and Liu (2020) develop linear poroe-
 183 lasticity using a weak Galerkin discretization of the mass balance and continuous Galerkin
 184 treatment of the momentum in deal.II (Bangerth et al., 2007). Among these efforts, the
 185 PyLith implementation appears to be unique in that it incorporates models of faults as
 186 dislocations in the elastic medium.

187 **2 Multiphysics Framework**

188 PyLith is designed to meet the needs of a wide range of users. Ease of use with ap-
 189 propriate defaults and seamless integration with mesh generation and visualization tools
 190 targets new users, whereas extensibility (Brown et al., 2015) targets advanced users need-
 191 ing custom features. Users can select finite-element discretizations to produce the dis-
 192 crete numerical representation of this system, and algebraic solvers to compute the so-
 193 lution. We strive to make it simple for outside contributors to alter the equations, ini-
 194 tial and boundary conditions, and material models defining a given geodynamics prob-
 195 lem. The poroelastic capability in PyLith is an example of such extensibility. In order
 196 to make this development possible, PyLith version 3 uses a new, extensible architecture

197 for governing equations, constitutive models, initial and boundary conditions, spatial dis-
 198 cretizations, and time stepping solvers. In this section, we describe these additions, us-
 199 ing the development of a poroelastic capability in PyLith as an example.

200 We draw from the mathematical notation in the PyLith User Manual and use sym-
 201 bols in bold to represent tensors, as in the example of the strain tensor, $\boldsymbol{\epsilon}$. We use over-
 202 head arrows to represent vector fields, as in the displacement vector \vec{u} . Scalar values are
 203 written in normal font, as in the example of porosity, ϕ .

204 **2.1 Finite-Element Discretization and Assembly**

205 PyLith follows the abstractions laid out for the finite-element method in (Ciarlet,
 206 1976) and (Kirby, 2004). These form the basis of modern finite-element frameworks, such
 207 as FEniCS (Logg et al., 2011) and Firedrake (Rathgeber et al., 2017). We compute the
 208 solution for displacement and pore pressure (u, p) using some approximation space \mathcal{P} .
 209 This space can be defined by an arbitrary basis, but it is usually a space of polynomi-
 210 als defined on each mesh cell and supplemented with continuity conditions at cell bound-
 211 aries. All tests presented here use the simple polynomial Lagrange spaces on simplex cells,
 212 P_k , and tensor product cells, Q_k . However, PyLith supports a much wider variety of spaces.
 213 The dual space \mathcal{P}' is a space of linear functionals or integrals we can compute using a
 214 function, e.g., the solution. Any measurement can be considered an integral of the in-
 215 put function, and thus the basis for this space can be represented by quadrature rules.
 216 These can be thought of as the discrete counterpart to Radon measures, which can rep-
 217 resent any linear functional according to the Riesz-Markov-Kakutani Theorem (Rowland,
 218 n.d.). The dual space allows us to define interpolation into our approximation space. Lastly,
 219 the reference cell \mathcal{K} is defined using the DMPlex mesh abstraction from PETSc (Knepley
 220 & Karpeev, 2009; Lange et al., 2016; Isaac & Knepley, 2017). Together these comprise
 221 a so-called *Ciarlet triple* $(\mathcal{P}, \mathcal{P}', \mathcal{K})$ and define our finite-element approximation.

222 PyLith uses these abstractions, so that users can easily change the default values
 223 for the finite-element discretization. For example, in the simulations settings for the full-
 224 scale Terzaghi benchmark for one-dimensional consolidation in a column, we set the ba-
 225 sis order (order of the finite-element approximation) for each solution field:

```
226 [pylithapp.problem.solution.subfields]
227 displacement.basis_order = 2
228 pressure.basis_order = 1
229 trace_strain.basis_order = 1
```

230 In fact, we can freely choose any finite element for a given field. Moreover, we can
 231 independently change the finite-element mesh, so that `basis_order = 2` results in a quadratic
 232 approximation space for both a mesh with triangular or tetrahedral cells, giving the P_2
 233 finite element, and a mesh with quadrilateral or hexahedral cells, giving the Q_2 finite el-
 234 element. We are also free to change the continuity requirements; for example, we can use
 235 discontinuous elements.

PyLith implements the assembly and application of finite-element operators as a hierarchical sequence following Knepley et al. (2013), a design that is also used in packages such as libCEED (Brown et al., 2021; Abdelfattah et al., 2021). We represent the assembly of residuals and Jacobians as the sum of sequences of weak form objects. The weak forms describe our conservation laws, constitutive equations, and initial and boundary conditions. We can write our finite-element residual evaluation as

$$\langle \phi, \vec{F}(\vec{u}) \rangle \sim \int_{\Omega} \phi \cdot f_0(\vec{u}, \nabla \vec{u}) + \nabla \phi : \vec{f}_1(\vec{u}, \nabla \vec{u}) = 0, \quad (2)$$

236 where the pointwise functions f_0, \vec{f}_1 capture the problem physics. The function \vec{F} is our
 237 residual function, which takes the approximate solution \vec{u} as an argument, and the func-
 238 tion ϕ , called a *test function*, is any function from our approximation space \mathcal{P} .

This approach can be extended to higher order derivatives by adding terms with additional pointwise functions, but PyLith is only concerned with C_0 finite-element methods, meaning methods enforce continuity of the basis functions, but not their derivatives, across cell boundaries. PETSc does allow purely local forms with higher derivatives in order to apply regularization, such as the Streamline-Upwind Petrov-Galerkin stabilization method (Brooks & Hughes, 1982). Discretizing the expression in Eq. (2), we have

$$\vec{F}(u) \sim \sum_e \mathcal{E}_e^T \left(\mathbf{B}^T \mathbf{W} f_0(\vec{u}^q, \nabla \vec{u}^q) + \sum_k \mathbf{D}_k^T \mathbf{W} \vec{f}_1^k(\vec{u}^q, \nabla \vec{u}^q) \right) = 0, \quad (3)$$

239 where \vec{u}^q is the vector of field evaluations at the set q of quadrature points on an ele-
 240 ment, \mathbf{W} is the diagonal matrix of quadrature weights, \mathbf{B} is the matrix of basis func-
 241 tion evaluations at quadrature points, \mathbf{D} the matrix of basis function derivative evalu-
 242 ations, and \mathcal{E}_e is the element restriction operator mapping coefficients from the global
 243 vector to the element vector. Using this model along with automated tabulation of ba-
 244 sis functions and derivatives at quadrature points, the user need only specify physics us-
 245 ing pointwise functions similar to the strong form of the governing equations. In this way
 246 we decouple the problem specification from mesh traversal (looping over cells) and lay-
 247 out of the degrees of freedom. This means that a PyLith user can write the physics ker-
 248 nels once, say for poroelasticity, and then use them with simplex or tensor product meshes
 249 and elements of different degree and type.

The Jacobian of Eq. (3) needs only derivatives of the pointwise functions,

$$\vec{F}'(u) \sim \sum_e \mathcal{E}_e^T \begin{bmatrix} \mathbf{B}^T & \mathbf{D}^T \end{bmatrix} \mathbf{W} \begin{bmatrix} f_{0,0} & f_{0,1} \\ \vec{f}_{1,0} & \vec{f}_{1,1} \end{bmatrix} \begin{bmatrix} \mathbf{B} \\ \mathbf{D} \end{bmatrix} \mathcal{E}_e, \quad [f_{i,j}] = \begin{bmatrix} \frac{\partial f_0}{\partial \vec{u}} & \frac{\partial f_0}{\partial \nabla \vec{u}} \\ \frac{\partial \vec{f}_1}{\partial \vec{u}} & \frac{\partial \vec{f}_1}{\partial \nabla \vec{u}} \end{bmatrix} (\vec{u}, \nabla \vec{u})$$

250 Thus we need four pointwise functions to specify the Jacobian of an expression, compared
251 to just two for the expression itself.

252 The pointwise functions for the residual are specified for each field in the solution,
253 whereas the pointwise functions for the Jacobian are specified for each pair of fields in
254 the solution. This allows sparsity to be preserved in element matrices, which can be cru-
255 cial for assembled matrices, but it does not allow reuse of possibly costly rheological com-
256 putations among fields. The pointwise functions for poroelasticity are given in Section 3.5.

257 The weak forms generally include integrals over the domain and boundaries. As
258 a result, we have pointwise functions for each of these integrals that capture the physics
259 of the governing equation, constitutive models, and boundary conditions. We also have
260 pointwise functions for updating the state variables and projecting the initial conditions
261 into the finite-element space. We use a small structure, called a `PetscFormKey`, to man-
262 age the association of pointwise functions with computation of the residuals and Jaco-
263 bians. The `PetscFormKey` specifies the domain associated with the pointwise function
264 using a `DMLabel` object (Balay et al., 2023a), which is capable of marking any set of mesh
265 points. We can mark subsets of the domain, even if disconnected, boundaries, interior
266 interfaces, collections of points, or unions of any of these sets. This gives us the ability
267 to identify the degrees of freedom that participate in the evaluation of the pointwise func-
268 tions. The key also specifies the field of the test function associated with the integral in
269 the weak form; in the case of the Jacobian, the key also includes the basis field. Finally,
270 the key specifies the an integer designating the part of the equation; PyLith uses this to
271 differentiate between implicit terms (terms on the left hand side of an equation) and ex-
272 plicit terms (terms on the right hand side of an equation) and differentiate between terms
273 associated with interior interfaces and subsets of the domain. However, a part number
274 could make arbitrary distinctions.

275 Once we have specified all pointwise functions using keys to identify how and where
276 they are used, PETSc divides the domain into regions, each supporting a subset of the
277 fields, constructs the necessary finite-element spaces and data layouts (embodied in `PetscSection`
278 objects (Balay et al., 2023a)), and lays out traversals of these regions. This gives the PETSc
279 library freedom to optimize the traversal, vectorize the low level operations, and perform
280 other optimization such as kernel fusion. Packages like LooPy (Klöckner, 2014) and libCEED

281 (Brown et al., 2021; Abdelfattah et al., 2021) are designed to take advantage of this struc-
282 ture.

283 **3 Physics Formulation**

284 We derive equations for the coupled flow and geomechanical system from conser-
285 vation and constitutive laws. We assume the fluids and solid matrix occupy the entire
286 domain (Bear, 1972; Coussy, 2005). We also assume that deformations are small, con-
287 ditions are isothermal, and the fluid is single phase and slightly compressible. In this pa-
288 per, we ignore inertia and use a quasi-static formulation.

289 The first documented solution in the field that would become poromechanics was
290 given by Terzaghi (von Terzaghi, 1923). Driven by the problem of soil consolidation, the
291 one-dimensional, empirical approach taken by Terzaghi acknowledged the need to cou-
292 ple deformation to pore fluid flow, with the assumption of incompressible solid and fluid
293 phases. A general theoretical treatment for elastic deformation of fluid bearing porous
294 media was first put forth by Biot in a study of soil consolidation (Biot, 1941). That work
295 assumed a linear elastic solid grain material, with incompressible pore fluid flow mod-
296 eled by Darcy’s Law, within the small strain formulation. Dynamic components of both
297 the conservation of mass and conservation of momentum terms were not considered, re-
298 sulting in a formulation commonly referred to as quasi-static.

299 Biot built upon his initial work, providing the theoretical foundation for the mod-
300 ern understanding of poroelasticity (Biot, 1956a). Touching on the portion relevant to
301 this study, Biot expanded the initial model of three-dimensional consolidation to the case
302 involving an anisotropic solid and a viscous, compressible fluid (Biot, 1955), as well as
303 that of a viscoelastic, anisotropic solid (Biot, 1956b). Additionally, he expanded the model
304 to wave propagation, reincorporating the dynamic components of the conservation equa-
305 tions, in a two parts, addressing the low frequency (Range & Biot, 1956) and high fre-
306 quency (Biot, 1956c) cases separately, with the ”low frequency” range referring to the
307 domain where Poiseuille flow may be assumed valid for pore fluid flow. Biot (1956b) also
308 pointed out an analogy between the equations of poroelasticity and the equations of ther-
309 moelasticity, stating that temperature in heat diffusion would play a similar role to fluid
310 pressure in the poroelastic fluid diffusion equation. However, thermoelastic problems solved
311 in an uncoupled fashion can produce acceptable results where a similarly simplified poroe-
312 lastic problem will not (Boley & Weiner, 2012; Boley, 1974). Later, Rice and Cleary (1976)
313 approached the problem of linear poroelasticity by treating it as an extension of the lin-
314 ear elastic case.

315

3.1 Conservation of momentum

The quasi-static assumption for displacement means that the momentum balance takes the same form as elastostatics,

$$\nabla \cdot \boldsymbol{\sigma}(\vec{u}, p, \epsilon_v) + \vec{f}(\vec{x}, t) = \vec{0}. \quad (4)$$

The body force term is often just the force of gravity on the combined system $\rho_b \vec{g}$, where we use the weighted average of the fluid density ρ_f and solid density ρ_s , called the bulk density ρ_b

$$\rho_b = \rho_s (1 - \phi) + \rho_f \phi, \quad (5)$$

316

using the porosity ϕ , the fraction of the porous medium occupied by the fluid. We can

317

also include other body force terms, such as tidal forcing or artificial forces used in test-

318

ing with the Method of Manufactured Solutions (Roache, 2002).

For a linearly elastic solid, we can write the Cauchy total stress tensor $\boldsymbol{\sigma}$ in the Biot model of poroelasticity as

$$\boldsymbol{\sigma} = \mathbf{C}_{dr} : \boldsymbol{\epsilon} - \alpha \mathbf{I} p, \quad (6)$$

where \mathbf{C}_{dr} is the drained elasticity tensor of rank four, $\boldsymbol{\epsilon}$ is the infinitesimal strain tensor with $\boldsymbol{\epsilon} = \frac{1}{2} (\nabla \vec{u} + \nabla^T \vec{u})$, and \mathbf{I} refers to the identity tensor of rank two. An isotropic, homogeneous, and linear poroelastic material, where we define Lamé's first parameter, λ , shear modulus, μ , and the Biot coefficient, α , has Cauchy total stress given by

$$\boldsymbol{\sigma} = \lambda \mathbf{I} \epsilon_v + 2\mu \boldsymbol{\epsilon} - \alpha \mathbf{I} p. \quad (7)$$

The terms not related to fluid pressure in the above relation may be combined to form the effective stress tensor ($\sigma'_{ij} = \lambda \delta_{ij} \epsilon_{ii} + 2\mu \epsilon_{ij}$), and the Lamé parameter λ is considered for the drained condition. We include the volumetric strain (trace strain),

$$\epsilon_v = \nabla \cdot \vec{u}, \quad (8)$$

319

as an unknown in order to maintain stability, as detailed later.

320

3.2 Conservation of mass

We only consider equations for the conservation of mass of the fluid phase, as we assume the mass of the solid phase remains constant. For a slightly compressible, single phase fluid within a poroelastic medium, with a stable, non-stress dependent value for permeability, the statement of conservation of mass is given by,

$$\dot{m} + \nabla \cdot \vec{w} = \rho_f \gamma. \quad (9)$$

321 where m denotes the fluid mass content defined as the fluid mass per unit bulk volume
 322 of porous medium, \vec{w} denotes the fluid mass flux with $\vec{w} = \rho_f \vec{q}$, ρ_f denotes the fluid
 323 density, \vec{q} denotes the fluid mass flow rate per unit area and time, and γ is the fluid vol-
 324 umetric source defined as the volume of injected fluid per unit porous media volume per
 325 unit time. This may also be expressed as the time derivative of the volume of injected
 326 fluid per unit of porous media volume ($\gamma = Q_t$).

In what follows, we assume that fluid density is uniform. Thus, we can divide the
 fluid conservation of mass equation by fluid density ρ_f , resulting in

$$\dot{\zeta} + \nabla \cdot \vec{q} = \gamma, \quad (10)$$

where ζ is the variation in fluid content and corresponds to the the amount of fluid vol-
 ume entering the solid per unit volume of solid. ζ may be expanded if we define the Biot
 modulus, M ,

$$\zeta = \frac{p}{M} + \alpha \epsilon_v. \quad (11)$$

The specific discharge vector \vec{q} , also referred to as the specific flux, corresponds to the
 volume of fluid that passes through a unit area of a porous medium per unit time. As
 we neglect inertia in this quasi-static formulation, we can write Darcy's law as

$$\vec{q} = -\frac{\mathbf{k}}{\mu_f} (\nabla p + \rho_f \vec{g}). \quad (12)$$

327 The specific flux corresponds to the time derivative of the specific relative fluid to solid
 328 displacement vector $\vec{d} = \phi (\vec{u}_f - \vec{u}_s)$, so that $\vec{q} = \dot{\vec{d}}$.

329 **3.3 Effective Stress Formulation**

330 In our poroelastic domain, the fluid phase occupies the pore space within the solid
 331 phase (Cheng, 2016). The governing equations enforcing conservation of mass and mo-
 332 mentum relate displacement of the solid phase, \vec{u} , and the fluid pressure, p . We assume
 333 small deformation (infinitesimal strain) and an isothermal system. In the formulation
 334 presented here, we also assume quasi-static conditions. That is, we neglect the inertial
 335 term in the momentum equation and fluid motion is purely diffusive. Currently, we have
 336 only included a linear elastic bulk rheology for the solid phase, with the intention to im-
 337 plement the viscoelastic bulk rheologies available in PyLith for the poroelastic formu-
 338 lation. Finally, we assume that the pore space is fully connected, the value for effective
 339 porosity is equivalent to the total porosity, and that the pore volume is fully saturated
 340 with a single phase, viscous, slightly compressible fluid.

The theory of poroelasticity as described by Biot (1941) makes use of two coupling
 coefficients, the Biot coefficient, α , and Biot modulus, M . The Biot coefficient represents

fluid volume change as a result of bulk volume change in the drained condition, and is expressed as

$$\alpha = 1 - \frac{K_{dr}}{K_s}, \quad (13)$$

341 where K_{dr} refers to the bulk modulus of the matrix of the drained porous medium, and
 342 K_s the bulk modulus of the solid phase. The “drained condition” in poroelasticity refers
 343 to the case where fluid pore pressure is at ambient pressure. In a poroelastic domain with
 344 a drained boundary, fluid is free to flow out, and the pore pressure at that boundary is
 345 considered to be zero. Thus, the bulk modulus of the drained state is a measure of the
 346 resistance to compression based solely from the material properties of the solid and the
 347 strength of the rock matrix. This contrasts with the bulk modulus for the “undrained”
 348 condition in which fluid pore pressure also accounts for resistance to compression, as the
 349 pore fluid is assumed to be confined within the rock. A Biot coefficient of one corresponds
 350 to an incompressible solid grain material and is the upper limit of possible values. Lower
 351 positive values indicate increasing compressibility of the solid phase.

The other coupling coefficient, Biot’s Modulus, M , is defined as the inverse of the constant strain storage coefficient, S_ϵ (Cheng et al., 2017), or the increase in the volume of fluid per volume of the solid phase that results from a unit increase in pore pressure under conditions of constant volumetric strain. For ease of adoption into our constitutive equation for fluid, we use the expression

$$\frac{1}{M} = \frac{\phi}{K_f} + \frac{\alpha - \phi}{K_s}, \quad (14)$$

352 where K_f refers to the bulk modulus of the pore fluid.

353 In order to maintain stability near the incompressible solid limit, we use a mixed-
 354 form discretization by including the volumetric strain, ϵ_v , as an unknown. Thus, our so-
 355 lution of the governing equations includes the displacement vector of the solid phase, \vec{u} ,
 356 fluid pore pressure, p , and the volumetric strain, ϵ_v .

Consolidation behavior of poroelastic media is bounded by two limiting cases of deformation mentioned earlier — drained, where deformation occurs under a constant pore fluid pressure, and undrained, where fluid flux across the control volume boundaries does not occur, resulting in no variation of fluid mass. Both of these end-member cases may be represented as elastic relations, given the insertion of the parameter appropriate for the drained or undrained case. The drained and undrained cases may also be understood as the limiting states of a porous medium subject to load. Drawing from the example of the constitutive equation for a linearly (poro)elastic, isotropic medium subject to a compressive load, the undrained case, applicable at $t = 0$ may be repre-

sented as

$$\boldsymbol{\sigma} = \left(K_u - \frac{2\mu}{3} \right) \mathbf{I}\epsilon_v + 2\mu\boldsymbol{\epsilon}, \quad (15)$$

and the drained case, applicable at $t \rightarrow \infty$

$$\boldsymbol{\sigma} = \left(K_{dr} - \frac{2\mu}{3} \right) \mathbf{I}\epsilon_v + 2\mu\boldsymbol{\epsilon}. \quad (16)$$

357 Some authors, e.g., Segall (2010), have approximated poroelastic effects by adjust-
 358 ing Poisson's ratio in purely elastic simulations. For example, a Poisson's ratio of close
 359 to 0.5 can approximate undrained conditions, and a Poisson's ratio closer to 0.25 can ap-
 360 proximate drained conditions. However, adjusting the Poisson's ratio does not capture
 361 the time dependence of the poroelastic deformation (McCormack et al., 2020). Thus, un-
 362 raveling the different physical processes potentially involved in postseismic deformation
 363 requires a fully coupled poroelastic model.

364 3.4 Strong Form

We create the strong form of our three-field poroelasticity formulation from the con-
 servation of momentum and mass in domain Ω with boundary Γ ,

$$\nabla \cdot \boldsymbol{\sigma}(\vec{u}, \epsilon_v, p) + \vec{f}(\vec{x}, t) = 0 \text{ in } \Omega, \quad (17)$$

$$\dot{\zeta}(\epsilon_v, p) + \nabla \cdot \vec{q}(p) - \gamma(\vec{x}, t) = 0 \text{ in } \Omega, \quad (18)$$

$$\nabla \cdot \vec{u} - \epsilon_v = 0 \text{ in } \Omega, \quad (19)$$

$$\boldsymbol{\sigma} \cdot \vec{n} = \vec{\tau}(\vec{x}, t) \text{ on } \Gamma_\tau, \quad (20)$$

$$\vec{u} = \vec{u}_0(\vec{x}, t) \text{ on } \Gamma_u, \quad (21)$$

$$\vec{q} \cdot \vec{n} = q_0(\vec{x}, t) \text{ on } \Gamma_q, \quad (22)$$

$$p = p_0(\vec{x}, t) \text{ on } \Gamma_p, \quad (23)$$

365 where $\boldsymbol{\sigma}$ is defined in Eq. (6), ζ is defined in Eq. (11), and \vec{q} is defined in Eq. (12). \vec{n} refers
 366 to the direction normal to a boundary, and the subscript zero refers to an initial con-
 367 dition. Time dependence in the problem is introduced solely through the loading con-
 368 ditions and constitutive models. A summary of the notation used to specify the prob-
 369 lem is given in Appendix Appendix A.

370 3.5 Weak form

The PETSc framework, which serves as the algebraic foundation of PyLith, solves
 systems of differential equations expressed in the form

$$\vec{F}(t, \vec{s}, \dot{\vec{s}}) = \vec{G}(t, \vec{s}), \quad (24)$$

where \vec{s} denotes the vector containing all solution fields. PyLith generates systems of algebraic equations having this form from assembly of the finite element weak form terms. Recalling the formulation from Eq. (2), we write

$$\int_{\Omega} \vec{\psi}^u \cdot \vec{f}_1(t, \vec{s}, \dot{\vec{s}}) + \nabla \vec{\psi}^u : \mathbf{f}_1(t, \vec{s}, \dot{\vec{s}}) d\Omega = \int_{\Omega} \vec{\psi}^u \cdot \vec{g}_0 + \nabla \vec{\psi}^u : \mathbf{g}_1(t, \vec{s}) d\Omega. \quad (25)$$

We solve the system of equations for our quasi-static formulation using the implicit time stepping methods provided by PETSc. For these methods it is convenient to put all terms on the left hand side of the equation so that we have $\vec{F}(t, \vec{s}, \dot{\vec{s}}) = \vec{0}$. We can write the residuals for the system of equations in the form

$$F^u(t, s, \dot{s}) = \int_{\Omega} \vec{\psi}^u \cdot \underbrace{\vec{f}(\vec{x}, t)}_{\vec{f}_0^u} + \nabla \vec{\psi}^u : \underbrace{-\boldsymbol{\sigma}(\vec{u}, p_f)}_{\mathbf{f}_1^u} d\Omega, \quad (26)$$

$$F^p(t, s, \dot{s}) = \int_{\Omega} \psi^p \underbrace{(\dot{\zeta}(\vec{u}, p_f) - \gamma(\vec{x}, t))}_{f_0^p} + \nabla \psi^p \cdot \underbrace{-\vec{q}(p_f)}_{\vec{f}_1^p} d\Omega + \int_{\Gamma_q} \psi^p \underbrace{[q_0(\vec{x}, t)]}_{f_0^p} d\Gamma, \quad (27)$$

$$F^\epsilon(t, s, \dot{s}) = \int_{\Omega} \psi^\epsilon \cdot \underbrace{(\nabla \cdot \vec{u} - \epsilon_v)}_{f^{\epsilon_0}} d\Omega. \quad (28)$$

371 The terms highlighted by the underbraces indicate the portions of the expressions im-
 372 plemented as point-wise functions in PyLith.

We compute the corresponding Jacobians using $J_F = \frac{\partial F}{\partial s} + t_{shift} \frac{\partial F}{\partial \dot{s}}$, where t_{shift} is a scalar determined by the time-stepping integration scheme and time step. For our three-field quasi-static formulation, we have nine potential Jacobian functions, of which

seven are nonzero,

$$J_F^{uu} = \frac{\partial F^u}{\partial u} + t_{shift} \frac{\partial F^u}{\partial \dot{u}} = \int_{\Omega} \psi^u_{i,k} \underbrace{(-C_{ikjl})}_{J_{f3}^{uu}} \psi^u_{j,l} d\Omega, \quad (29)$$

$$J_F^{up} = \frac{\partial F^u}{\partial p} + t_{shift} \frac{\partial F^u}{\partial \dot{p}} = \int_{\Omega} \psi^u_{i,j} \underbrace{(\alpha \delta_{ij})}_{J_{f2}^{up}} \psi^p d\Omega, \quad (30)$$

$$J_F^{u\epsilon_v} = \frac{\partial F^u}{\partial \epsilon_v} + t_{shift} \frac{\partial F^u}{\partial \dot{\epsilon}_v} = \int_{\Omega} \psi^u_{i,j} \underbrace{(-\lambda \delta_{ij})}_{J_{f2}^{u\epsilon_v}} \psi^{\epsilon_v} d\Omega, \quad (31)$$

$$J_F^{pu} = \frac{\partial F^p}{\partial u} + t_{shift} \frac{\partial F^p}{\partial \dot{u}} = 0, \quad (32)$$

$$J_F^{pp} = \frac{\partial F^p}{\partial p} + t_{shift} \frac{\partial F^p}{\partial \dot{p}} = \int_{\Omega} \underbrace{\psi_{trial,k}^p \left(\frac{\mathbf{k}}{\mu_f} \delta_{kl} \right)}_{J_{f3}^{pp}} \psi_{basis,l}^p d\Omega + \int_{\Omega} \underbrace{\psi^p \left(t_{shift} \frac{1}{M} \right)}_{J_{f0}^{pp}} \psi^p d\Omega, \quad (33)$$

$$J_F^{p\epsilon_v} = \frac{\partial F^p}{\partial \epsilon_v} + t_{shift} \frac{\partial F^p}{\partial \dot{\epsilon}_v} = \int_{\Omega} \underbrace{\psi^p (t_{shift} \alpha)}_{J_{f0}^{p\epsilon_v}} \psi^{\epsilon_v} d\Omega, \quad (34)$$

$$J_F^{\epsilon_v u} = \frac{\partial F^{\epsilon_v}}{\partial u} + t_{shift} \frac{\partial F^{\epsilon_v}}{\partial \dot{u}} = \int_{\Omega} \underbrace{\psi^{\epsilon_v} (\delta_{ij})}_{J_{f1}^{\epsilon_v u}} \psi^u_{i,j} d\Omega, \quad (35)$$

$$J_F^{\epsilon_v p} = \frac{\partial F^{\epsilon_v}}{\partial p} + t_{shift} \frac{\partial F^{\epsilon_v}}{\partial \dot{p}} = 0, \quad (36)$$

$$J_F^{\epsilon_v \epsilon_v} = \frac{\partial F^{\epsilon_v}}{\partial \epsilon_v} + t_{shift} \frac{\partial F^{\epsilon_v}}{\partial \dot{\epsilon}_v} = \int_{\Omega} \underbrace{\psi^{\epsilon_v} (-1)}_{J_{f0}^{\epsilon_v \epsilon_v}} \psi^{\epsilon_v} d\Omega. \quad (37)$$

373 The detailed derivation can be found in Appendix Appendix F.

374 3.6 Solvers

375 In our quasi-static formulation of poroelasticity, we use an implicit formulation to
 376 enforce conservation of momentum at each timestep. For the linear systems, we use a
 377 basic Schur complement solver (May & Moresi, 2008; Brown et al., 2012), which couples
 378 displacement and trace strain, and then finds the Schur complement against pressure.
 379 It is also possible to do this split nonlinearly (Brune et al., 2015); however, we have not
 380 yet implemented this feature.

381 The full scale tests shown in Section 4.2 have an impulsive start, meaning that fi-
 382 nite force or traction is suddenly switched on at time zero. This is necessary for the an-
 383 alytic solution but causes problems evaluating temporal convergence since it appears as
 384 a ramp when discretized. In the simulations in Section 4.2 we configure the adaptive timestep
 385 selector in PETSc to take very small initial timesteps so that all simulations for each test
 386 case have the same initial ramp for the applied loading. This allows clear determinations
 387 of the temporal convergence exponent.

388 4 Verification of Numerical Implementation

389 We verify our numerical implementation using both analytical and manufactured
 390 solutions. We use the Method of Manufactured Solutions to check our finite-element im-
 391 plementation of the governing equations. We use full-scale tests with analytical solutions
 392 to check the complete simulation workflow, including input and output.

393 4.1 Method of Manufactured Solutions

394 To verify the accuracy of our multiphysics code, we use the method of manufac-
 395 tured solutions (Roache, 2002; Oberkampf et al., 2004). This approach allows us to ver-
 396 ify the order of accuracy of our discretization and convergence of the solution. The pro-
 397 cess involves generating solutions of sufficient complexity to allow for rigorous testing
 398 of all aspects of the governing equations. The solution in this case is a purely mathemat-
 399 ical exercise, and solutions may be designed solely for ease of analytical manipulation.
 400 A common approach for a method of manufactured solutions test is to use a smooth an-
 401 alytical function for the solution and compute an artificial body force so that the solu-
 402 tion satisfies the governing equations when the body force is included.

403 We evaluate the accuracy of our implementation using the method of manufactured
 404 solutions in four ways:

- 405 1. Representation of the solution in the finite-element space;
- 406 2. Residual for the exact solution is smaller than some tolerance;
- 407 3. The linear model converges to the residual action at second-order; and
- 408 4. A finite-difference Jacobian matches the computed Jacobian.

First, we verify that we can represent the solution for the method of manufactured solutions in the finite-element space. That is,

$$\|\vec{s}^* - \vec{s}\| \leq \epsilon, \quad (38)$$

where \vec{s} is the solution in the finite-element space, \vec{s}^* is the analytical solution, and ϵ is some small tolerance. Second, we verify the residual for the solution \vec{s} is below some tolerance, ϵ ,

$$\|F(\vec{s}) - G(\vec{s})\| \leq \epsilon, \quad (39)$$

where $F(\vec{s})$ is the left hand side residual and $G(\vec{s})$ is the right hand side residual (in these tests $G(\vec{s}) = \vec{0}$). In the Taylor series test for the Jacobian J , we verify that

$$\|F(\vec{s} + \delta\vec{v}) - F(\vec{s}) - \delta J(\vec{s})\vec{v}\| < C\delta^2, \quad (40)$$

Test Name	Displacement		Pore Pressure		Trace Strain	
	Space	Time	Space	Time	Space	Time
S2T1	quadratic	linear	linear	linear	linear	linear
S2Tt	quadratic	trig	linear	trig	linear	trig
StT1	trig	linear	trig	linear	trig	linear

Table 1: Spatial and temporal functions used in the method of manufactured solutions test cases. linear: 1st order polynomial; quadratic: 2nd order polynomial; trig: trigonometric function. For S2T1 our approximation space contains the analytical solution, so the finite-element approximation is exact (within machine precision).

409 where \vec{v} is a unit perturbation to the solution and C is some constant independent of
410 \vec{v} . For the finite difference test we compute the Frobenius norm (root mean square of
411 the matrix elements) of the difference between the analytical and finite difference Jaco-
412 bians.

413 For a given method of manufactured solutions test case, we provide

- 414 • Analytical functions for each subfield of the solution;
- 415 • Analytical functions for each input field (e.g., material properties);
- 416 • Analytical functions for each Dirichlet boundary condition; and
- 417 • Finite-element discretization.

418 For the quasi-static poroelastic coupled problem in PyLith, we perform method of man-
419 ufactured solutions tests for three sets of exact solutions in both two and three-dimensions,
420 defined by the type of functions we use for the spatial and temporal variation. Table 1
421 shows the different functions we use in the solution for our method of manufactured so-
422 lutions tests. Section Appendix B contains the expressions for all of the analytical func-
423 tions for each method of manufactured solutions test.

424 Figs. 1–3 show the solution for S2T1 along with the error, which should be machine
425 precision as the functions exist in our finite element space. Figs. 4 and 5 show mesh con-
426 vergence for our method, in both space and time. For spatial convergence, we use the
427 StT1 solution, and meshes on the unit square ranging from 128 to 8192 triangles. For
428 temporal convergence, we use the S2Tt solution run for 5 timesteps, using timesteps rang-
429 ing from 0.1 to 0.0125.

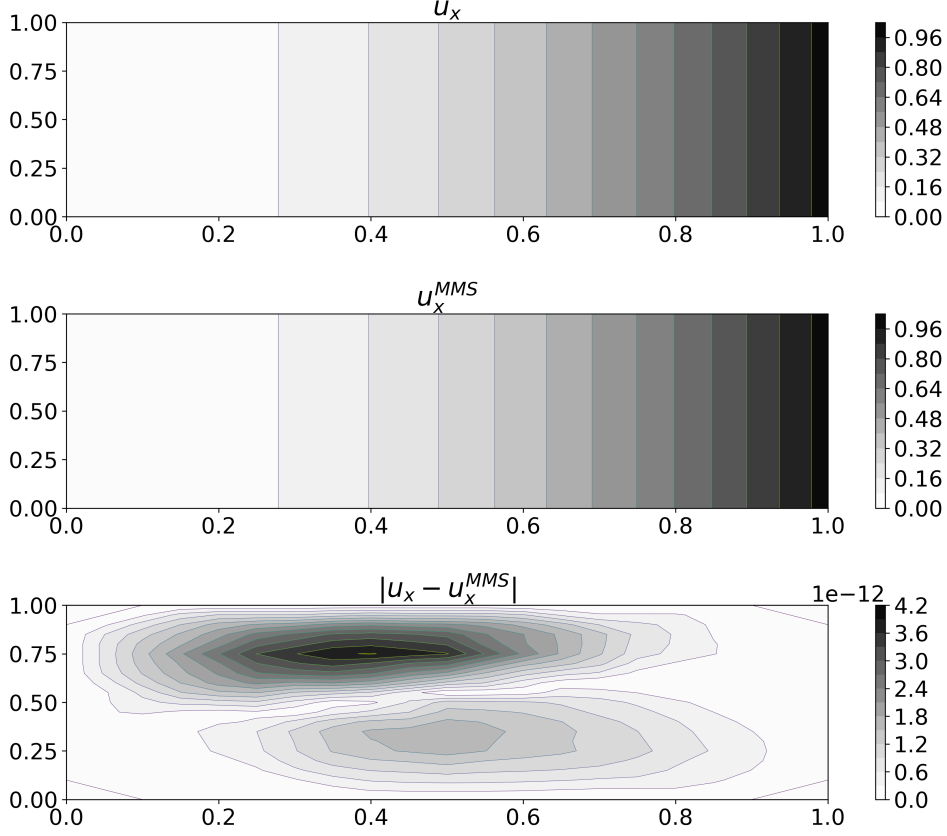


Figure 1: Plot of the x displacement component solution field for the two-dimensional method of manufactured solution test with a manufactured solution that varies quadratically with respect to space and linearly with respect to time (S2T1). A full derivation of the solution is available in Appendix B1. As our goal is to test the functionality of our physics implementation, we pick a solution that is easily differentiable, ignore units, and set all coefficient values to unity, with the exception of λ that is set to a value of $\frac{2}{3}$. The first row shows the computed solution, the second row shows the analytic solution, and the third row shows the error. As evidenced by plot of the error, we find a good fit between the analytical and numerical solutions.

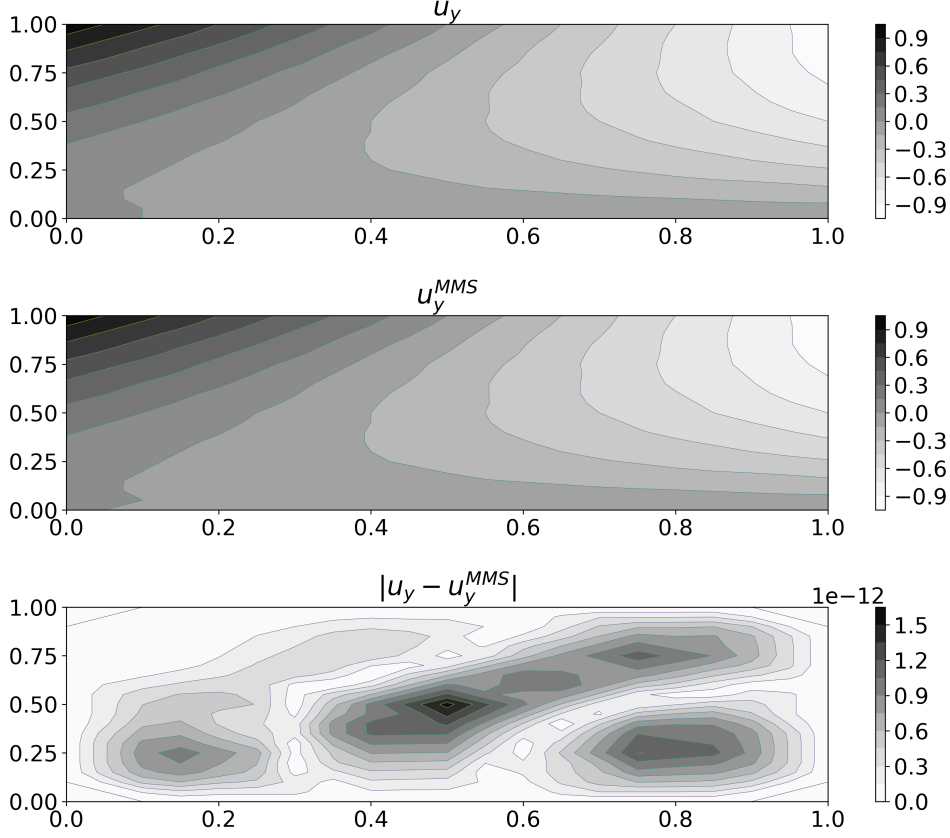


Figure 2: Plot of the y displacement component solution field for the two-dimensional method of manufactured solution test with a manufactured solution that varies quadratically with respect to space and linearly with respect to time (S2T1). A full derivation of the solution is available in Appendix B1. As our goal is to test the functionality of our physics implementation, we pick a solution that is easily differentiable, ignore units, and set all coefficient values to unity, with the exception of λ that is set to a value of $\frac{2}{3}$. The first row shows the computed solution, the second row shows the analytic solution, and the third row shows the error. As evidenced by plot of the error, we find a good fit between the analytical and numerical solutions.

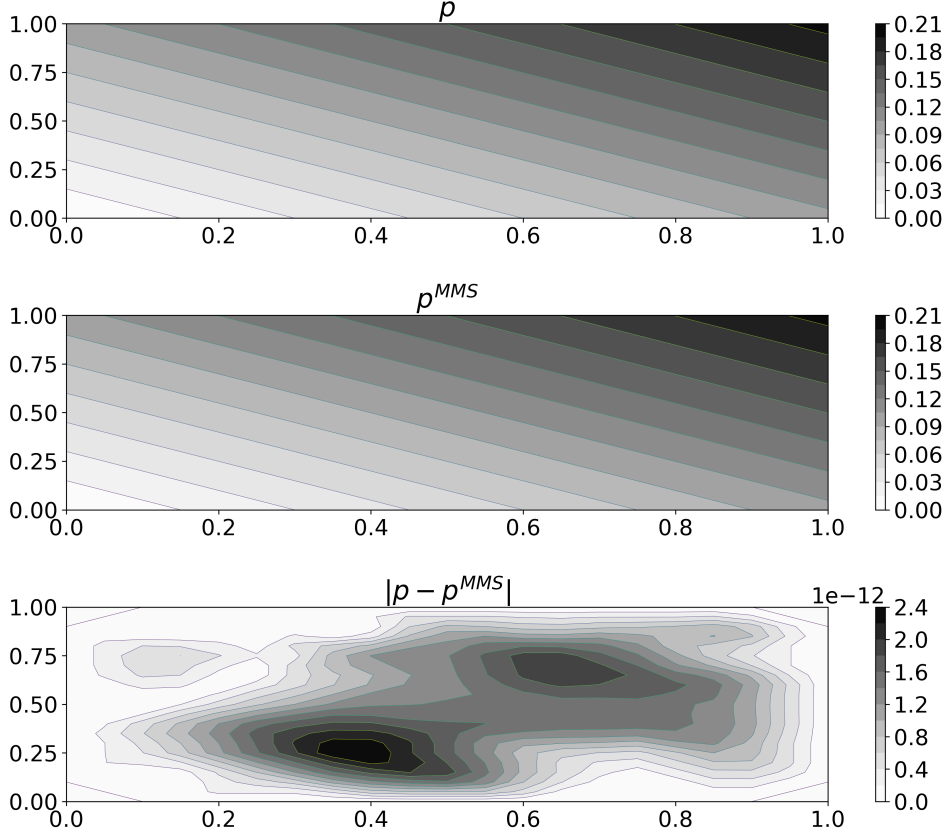


Figure 3: Plot of the pressure solution field for the two-dimensional method of manufactured solution test with a manufactured solution that varies quadratically with respect to space and linearly with respect to time (S2T1). A full derivation of the solution is available in Appendix B1. As our goal is to test the functionality of our physics implementation, we pick a solution that is easily differentiable, ignore units, and set all coefficient values to unity, with the exception of λ that is set to a value of $\frac{2}{3}$. The first row shows the computed solution; the second row shows the analytic solution; and the third row shows the error. As evidenced by plot of the error, we find a good fit between the analytical and numerical solutions.

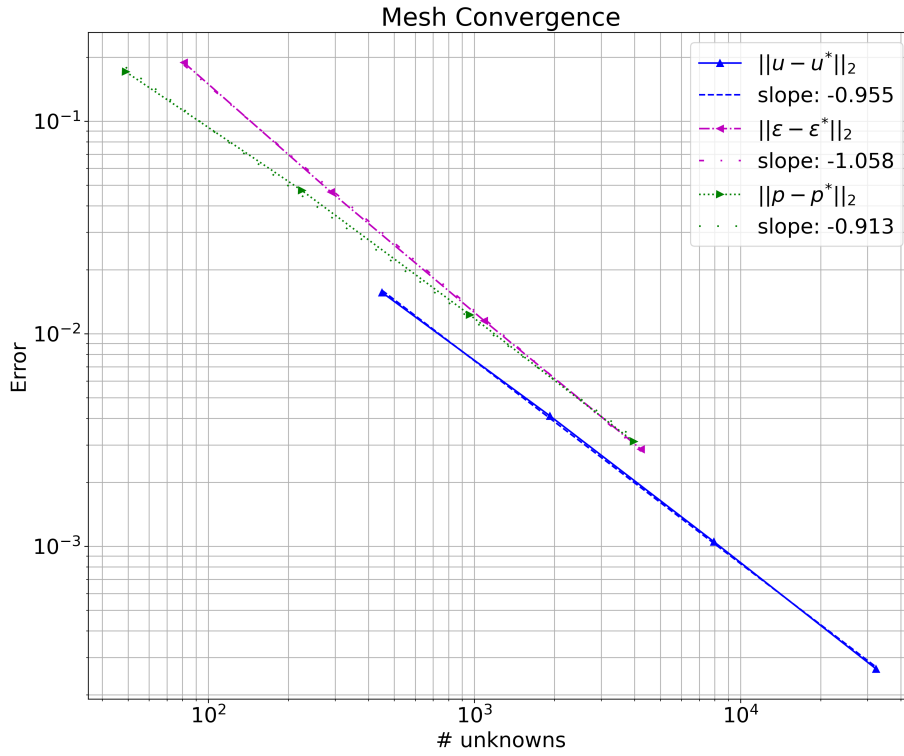


Figure 4: Plot of mesh convergence for the StT1 method of manufactured solutions solutions. We observe the expected rate of spatial convergence for displacement and superconvergence for pressure, due to the symmetric nature of the solution. Note that the slope is half the convergence rate as we plot against the problem size N rather than resolution h .

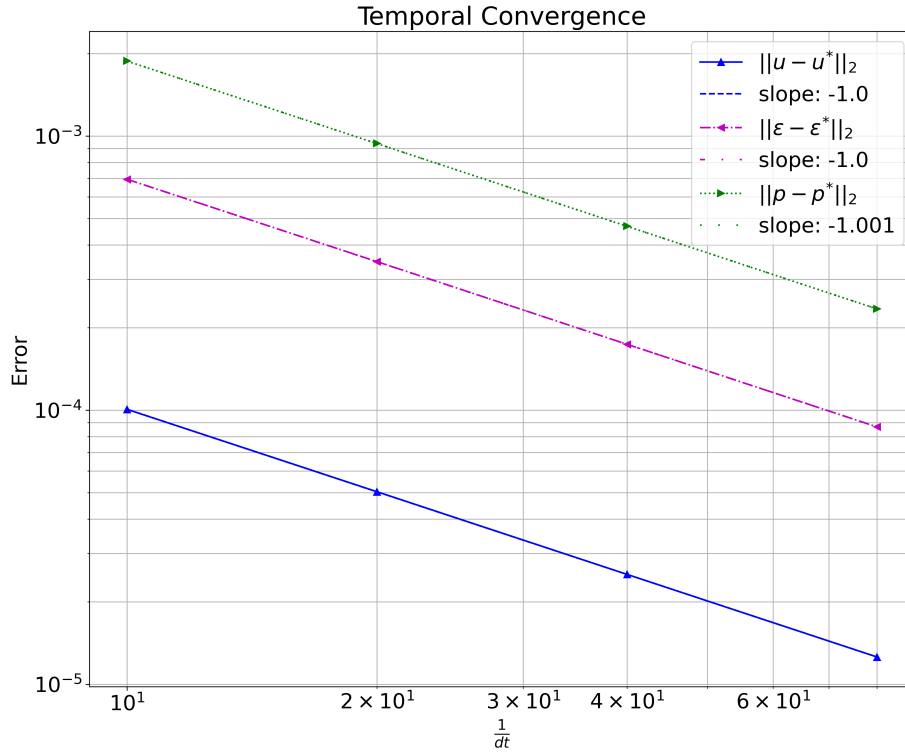


Figure 5: Plot of temporal convergence for the S2Tt method of manufactured solutions. We observe the expected linear rate of temporal convergence for the Backward Euler integrator.

4.2 Full-Scale Analytical Test Cases

We also test the poroelasticity implementation using full-scale (complete) simulations. We select three problems with well-resolved analytical solutions that frequently appear as published benchmarks for poroelastic numerical implementations (Coussy, 2005; Selvadurai, 2007; Meng, 2017). The problems are the one-dimensional Terzaghi consolidation problem, the two-dimensional Mandel problem, and the three-dimensional Cryer problem. We model the first two problems using a two-dimensional domain and the third with a three-dimensional spherical domain.

All three problems test important features of the poroelasticity implementation, such as Dirichlet and Neumann boundary conditions for displacement and pore pressure, in addition to the governing equations. We run all tests discussed in the following sections using continuous Lagrange elements with a second-order discretization for displacement and first-order discretizations for trace strain and pressure. For each problem we look at the reduction in error as the mesh resolution increases. We evaluate the error using the exact solution.

4.2.1 Terzaghi's Problem

The one-dimensional consolidation problem was first presented by Terzaghi (von Terzaghi, 1923). The problem is drawn from uniaxial compaction of a soil sample. Terzaghi recognized that compressive stress acting on a soil sample would face resistance from pore fluid pressure and formulated a concept of effective stress. We consider a two-dimensional domain; however, the simple geometry allows a one-dimensional analytical solution. Unlike Terzaghi's original work, we do not consider the solid grain as incompressible, so we include the Biot coefficient in our effective stress relation.

An initially undisturbed soil sample of a thickness L along the y axis rests upon a rigid, impermeable base (Fig. 6). The sample is laterally constrained, restricting displacement in the x direction to zero and prohibiting flow through the x axis boundaries. The top boundary of the sample is "drained" with respect to the fluid pore pressure, meaning that fluid pore pressure is considered to be equal to ambient conditions and fluid flow is unhindered. At the top boundary, where $y = L$, we apply a uniform compressive stress σ_{zz} at $t = 0$, incurring an instantaneous pore pressure rise within the material to the undrained value. As the compressive load is maintained, the drainage occurs through the top boundary, and the sample contracts in the direction of the applied load. Fig. Appendix C contains the analytical solutions for pore pressure and displacement.

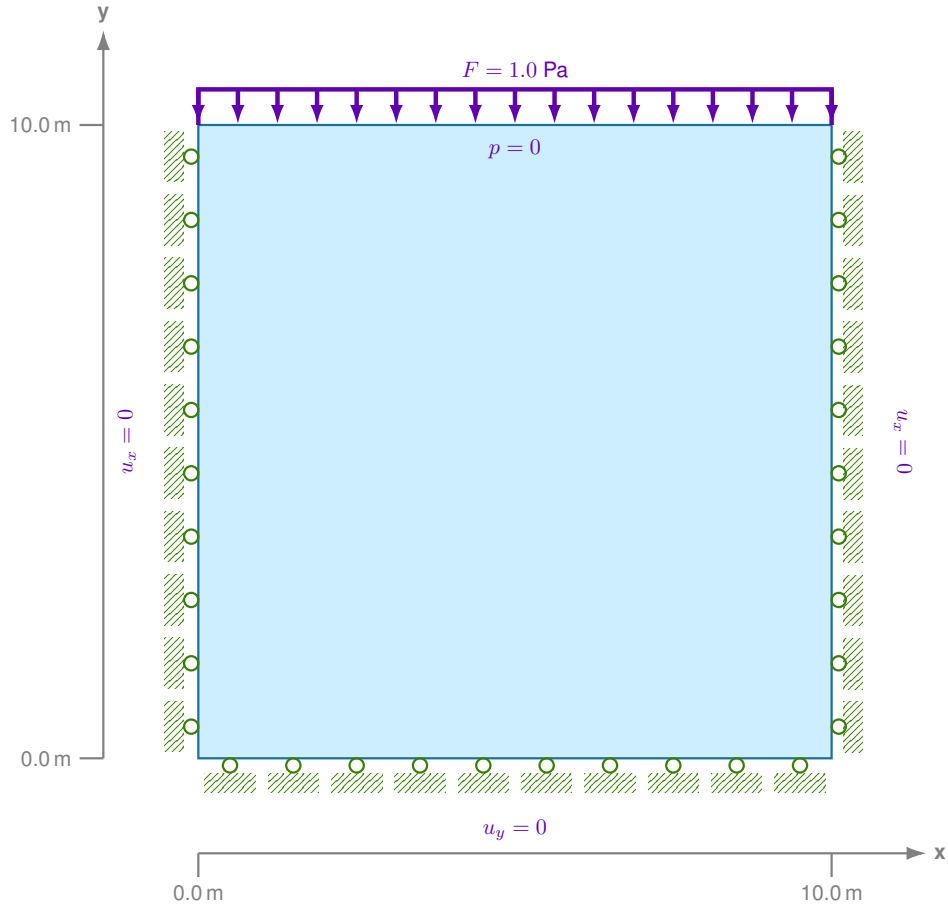


Figure 6: Terzaghi's problem for uniaxial consolidation. We consider a poroelastic domain, 10 m in width. It is subject to a uniform compressive force of 1.0 Pascal applied at the top boundary. The top boundary is simultaneously modeled as drained, meaning that the pressure at the boundary is kept at ambient conditions, permitting flow out of the domain. The domain is resting on a rigid base. The analytical solution, found in Appendix Appendix C, is one dimensional; however, we model the problem as two-dimensional and include roller conditions at the left and right domain boundaries.

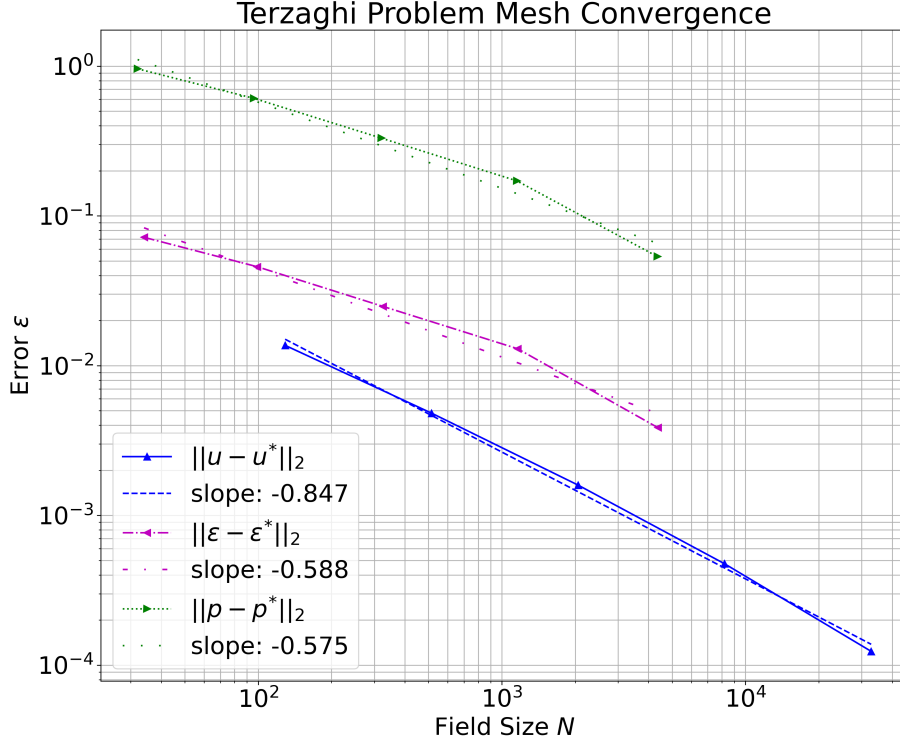


Figure 7: Mesh convergence for Terzaghi’s problem. The displacement, u , error is shown first, with the points represented with triangles pointing up. The trace strain, ϵ error is drawn with triangles pointing left. The pressure, p , error is drawn with triangles pointing right. We obtain the expected rate of convergence of these fields.

463 We select material parameters for our Terzaghi benchmark for the benefit of sim-
 464 plicity as opposed to realistic conditions, consistent with other recent benchmarking ef-
 465 forts (Cheng, 2016; Jha & Juanes, 2014; Meng, 2017). We use a fluid viscosity of 1 Pa-
 466 s, a porosity of 0.1, a Biot coefficient of 0.6, a shear modulus of 3.0 Pa, a drained bulk
 467 modulus of 4.0 Pa, a fluid bulk modulus of 8.0 Pa, a solid bulk modulus of 10.0 Pa, and
 468 an isotropic permeability of $1.5 M^2$. We use a square domain that is 10 m in length. We
 469 discretize our domain using identically sized quadrilateral elements with a nominal size
 470 of 1.0 m. We refine the mesh up to four times to create meshes ranging from about 100
 471 cells to 100,000 cells to check the rate of convergence.

472 In Fig. 7, we see that the Terzaghi solution closely matches the analytic results and
 473 exhibits mesh convergence. We obtain second-order convergence for displacement and
 474 first-order for pressure. These are the expected rates for this finite element (Mardal et
 475 al., 2021). Since this problem has an impulsive start, the initial rise in pressure will be

476 smeared over the first timestep, which accounts for a large part of the temporal error.
 477 In order to measure this accurately, we fix the size of the first timestep at 10^{-5} . For spa-
 478 tial convergence tests, all timesteps are also the same size. We start with a mesh 2 cells
 479 wide and 32 cells long, which is regularly refined four times during the test. Because we
 480 show error plotted against the number of degrees of freedom, the slope of our line is $-\alpha/d$,
 481 where α is the rate of convergence and d is the spatial dimension. Material and mesh
 482 parameters may be found in the Terzaghi full-scale test directory `tests/fullscale/poroelasticity/`
 483 `terzaghi` within the PyLith source code (Aagaard, Knepley, & Williams, 2022a). In Figs. 8
 484 and 9 we also show the solutions for pressure and displacement, respectively, at select
 485 times in the evolution. We can see the pulse of pressure at the initial time decay away
 486 as the column slowly compresses.

487 **4.2.2 Mandel’s Problem**

488 Mandel’s problem (Mandel, 1953) was one of the first published solutions to demon-
 489 strate non-monotonic pressure behavior, characteristic of poroelastic response. This dif-
 490 fers from Terzaghi’s problem, where pressure was treated as uncoupled from solid de-
 491 formation. The problem consists of a rectangular domain compressed between two rigid,
 492 frictionless plates (Fig. 10). The domain is assumed to be infinitely long along the z axis,
 493 resulting in plane strain conditions. We assume the domain is homogeneous; however,
 494 extensions of Mandel’s problem to include anisotropy exist (Abousleiman et al., 1996).
 495 Lateral edges are unconfined and maintained at a drained condition, with pore pressure
 496 equal to zero. At time $t = 0$, a compressive vertical pressure of F is applied to both
 497 confining plates. At initial application of compressive force, vertical stress σ_{yy} is uniform
 498 across the domain. Along the lateral edges, however, the subsequent pore pressure in-
 499 crease quickly interacts with the drained boundary condition, resulting in a softening of
 500 the material along the lateral edges and a transfer of vertical stress toward the center
 501 of the domain. This results in a further increase in pore pressure toward the center of
 502 the domain that eventually dissipates as the domain drains. This phenomenon is referred
 503 to as the "Mandel-Cryer Effect" (Cryer, 1963).

504 We exploit the symmetry of the problem and only model a quarter of the domain
 505 (Fig. 11). We impose impermeable roller boundaries on the $-x$ and $-y$ boundaries and
 506 apply uniform compression to an impermeable plate on the $+y$ boundary. On the remain-
 507 ing ($+x$) boundary, we impose a traction free condition maintained at the drained con-
 508 dition (zero pressure). We assume that the domain is infinitely long in the z direction,
 509 and that the plane strain condition is valid for that axis (Cheng, 2016). We choose a rect-
 510 angular domain that is 1.0 m by 10 m, and choose quadrilateral elements of a uniform

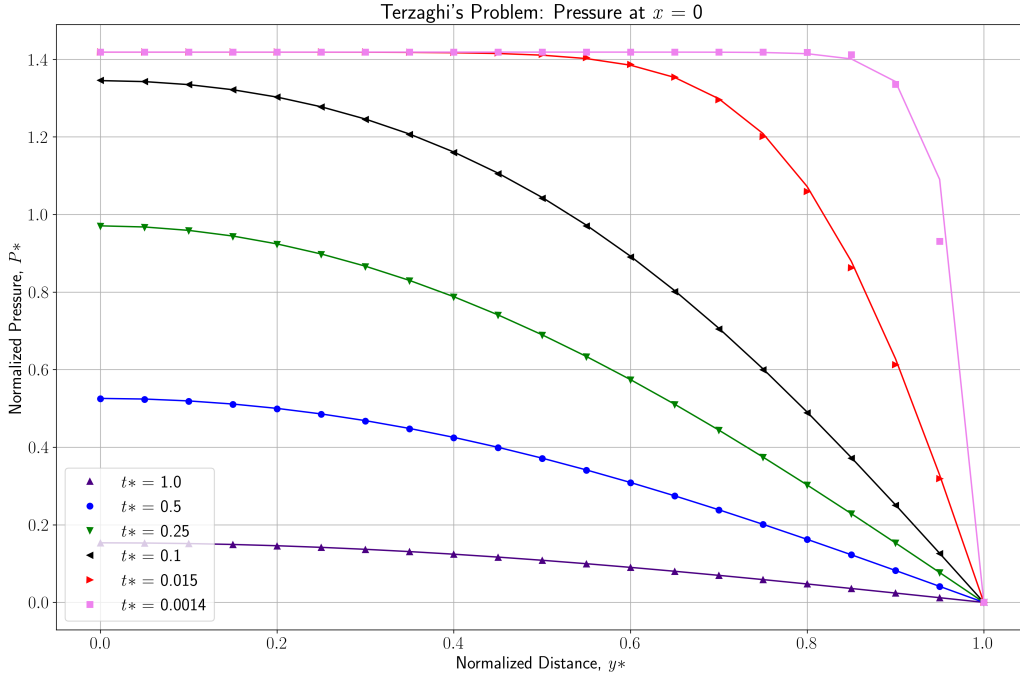


Figure 8: Representation of normalized pressure values over time for the Terzaghi problem. As the solution is one dimensional, we choose to display normalized pressure ($p^* = \frac{p}{p_0}$, where p_0 is the absolute value of the compressive force, F) along a vertical slice along the left boundary, where $x = 0$. This is plotted over a normalized length, $y^* = \frac{y}{L}$, where L is the width along the y axis. These are plotted for normalized time snapshots, $t^* = \frac{ct^2}{L^2}$, with the consolidation coefficient, c , defined in Appendix A2. We plot numerical results as a continuous line with analytical solutions at discrete points represented by shape overlays. The shapes representing analytical solutions are varied with regard to the normalized time that they represent. We find a good fit between the numerical and analytical solutions.

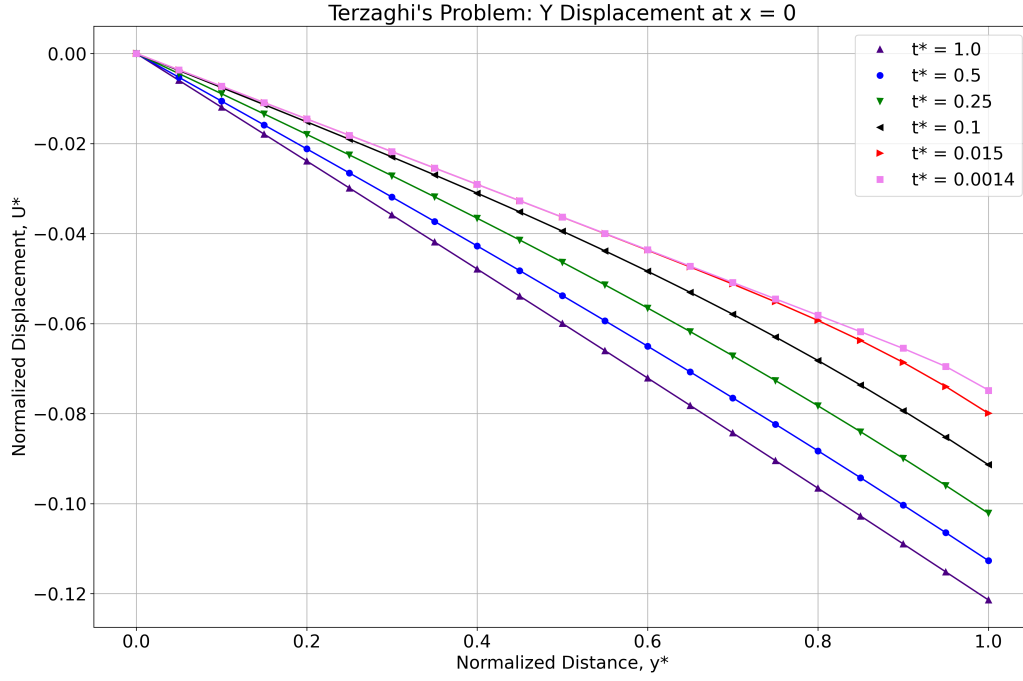


Figure 9: Representation of normalized displacement values over time for the Terzaghi problem. As the solution is one dimensional, we are concerned only with displacement in the y direction (consolidation). We consider compression as negative and display the normalized y component displacement along vertical slice following the left boundary, where $x = 0$. This is plotted over a normalized length, $y^* = \frac{y}{L}$, where L is the width along the y axis. These are plotted for normalized time snapshots, $t^* = \frac{ct^2}{L^2}$, with the consolidation coefficient, c , defined in Appendix A2. We plot numerical results as a continuous line with analytical solutions at discrete points represented by shape overlays. The shapes representing analytical solutions are varied with regard to the normalized time that they represent. The results show that consolidation decreases with depth and displays a good fit between the numerical and analytical solutions.

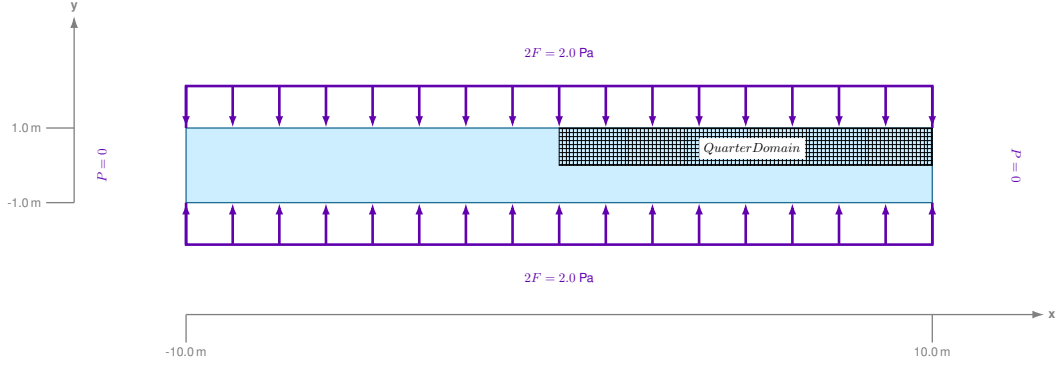


Figure 10: Diagram of Mandel’s full problem. A homogeneous, poroelastic slab is contained between two impermeable and frictionless plates. This slab is considered to be of infinite length in the z axis direction (out toward the reader) and is considered under a generalized plane strain condition ($u_z = 0$ and $q_z = 0$.) The boundaries in the positive and negative x axis directions are stress free and drained (held at ambient pressure), resulting in outflow from the slab. Owing to the symmetry of the problem, we need only consider a quarter of the domain, shaded and labeled here. We expand upon our quarter domain problem in Fig. 11.

511 size for our mesh. The nominal mesh contains 160 elements, each with edge lengths of
 512 0.5 m. We refine the mesh up to four times to create meshes with up to about 10,000
 513 cells to check the rate of convergence.

514 We again provide the analytical solutions in Appendix Appendix D. We assume
 515 the same material properties as in the Terzaghi example. From Figs. 12–14, the com-
 516 puted solution closely matches the analytical solution. Fig. 15 shows that we do not quite
 517 achieve second-order convergence, which we attribute to the inaccuracy of resolving the
 518 impulsive start. The pressure exhibits first-order convergence, which matches the expected
 519 rate for the first-order approximation space. Material and mesh parameters may be found
 520 in the Mandel full-scale test directory `tests/fullscale/poroelasticity/mandel` within
 521 the PyLith source code (Aagaard, Knepley, & Williams, 2022a).

522 **4.2.3 Cryer’s Problem**

523 Cryer (1963) studied the problem of a saturated sphere of porous material subjected
 524 to a compressive traction on the surface. The surface is maintained at the drained con-
 525 dition, allowing fluid to freely escape (see Fig. 16). Owing to the Skempton effect (Skempton,
 526 1954), the pore pressure in the domain will rise from an initial, uniform value, before de-
 527 creasing as a result of pressure diffusion through the surface boundary. This non-monotonic

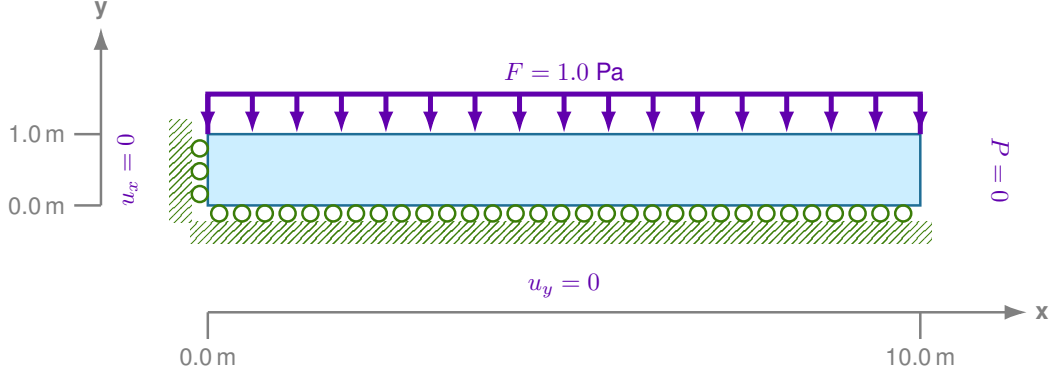


Figure 11: Owing to the symmetry of the problem outlined in Fig. 10, we consider a quarter domain reduced problem. The quarter domain is limited to a single stress free, drained boundary along the positive x axis edge of the domain. The overall compressive force is halved, as it acts over a y positive boundary with half the length of the full problem. We restrict displacement in the x direction along the left boundary at $x = 0$, along with displacement in the y direction along the bottom boundary at $y = 0$.

528 pressure behavior is, once again, known as the Mandel-Cryer effect. The spherical do-
 529 main, along with uniform compression at the surface, permits a three-dimensional poroe-
 530 lastic compaction problem to be represented as a pair of one-dimensional equations for
 531 pressure and displacement in spherical coordinates with closed form analytical solutions
 532 (see Appendix Appendix E). Making use of the symmetry of the problem, we model one
 533 eighth of the sphere, with zero displacement boundary conditions along the truncated
 534 boundaries as shown in Fig. 17.

535 We use the same discretization and material properties as in the previous two bench-
 536 marks. We conduct our test on a spherical section of a sphere with a radius of 1.0 m.
 537 Our nominal mesh consists of 896 hexahedral elements with edge lengths of about 0.1
 538 m. Complete material and mesh parameters may be found in the Cryer full-scale test
 539 directory `tests/fullscale/poroelasticity/cryer` within the PyLith source (Aagaard,
 540 Knepley, & Williams, 2022a).

541 In Fig. 18, we plot the normalized pressure, $p^* = \frac{p}{F}$ where F is radial compressive
 542 stress on the domain, at the origin of the eighth domain Cryer problem benchmark.
 543 We observe the Mandel-Cryer effect, although we overestimate pressure rise due to our
 544 finite timestep. The overestimation can also be seen in Fig. 19, where we plot the pres-
 545 sure radially. As the pressure relaxes, we converge to the true solution.

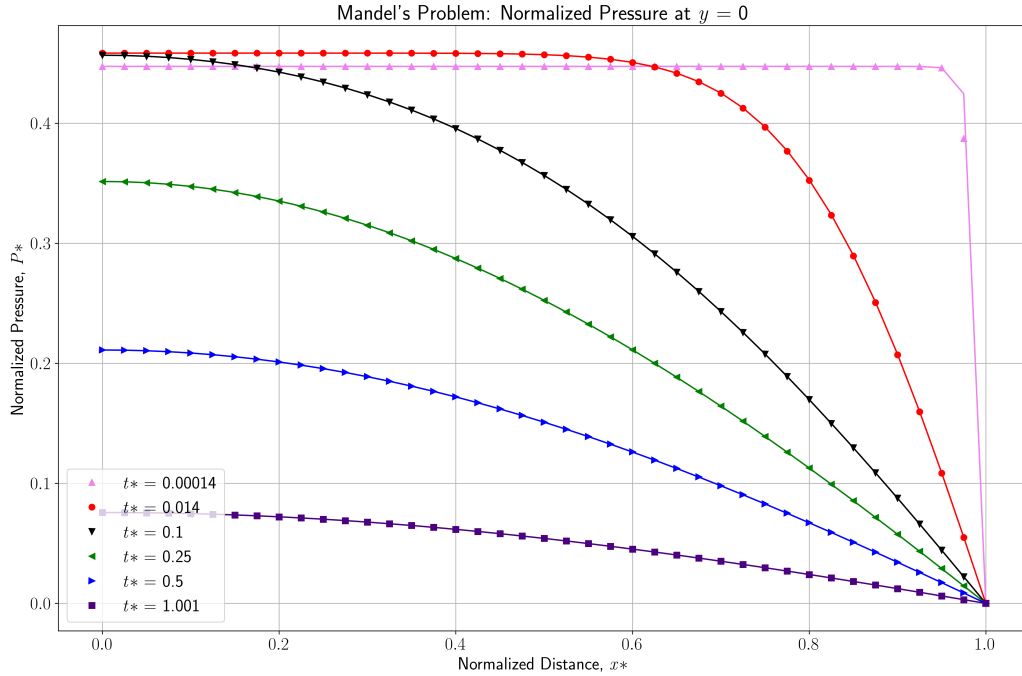


Figure 12: Normalized pressure results for a horizontal line drawn where $y = 0$ for a mesh consisting of quadrilateral elements. We define normalized pressure as $p^* = \frac{ap}{F}$, where a is the length of the quarter domain along the x axis. Normalized distance along the x axis is defined as $x^* = \frac{x}{a}$. We define dimensionless time as $t^* = \frac{ct}{a^2}$, with the definition for the consolidation coefficient, c , defined in Table ???. In contrast to the pressure results in Fig. 8, we observe non-monotonic pressure behavior in the early time, with pressure nearer to the center of the domain increasing above the initial value for a short period of time. This behavior is referred to as the "Mandel-Cryer" effect. Results generated by our numerical simulation are represented as continuous lines with analytical solution results plotted as shapes at discrete points. The shapes representing analytical solutions are varied with regard to the normalized time that they represent. We observe excellent agreement between numerical and analytical results.

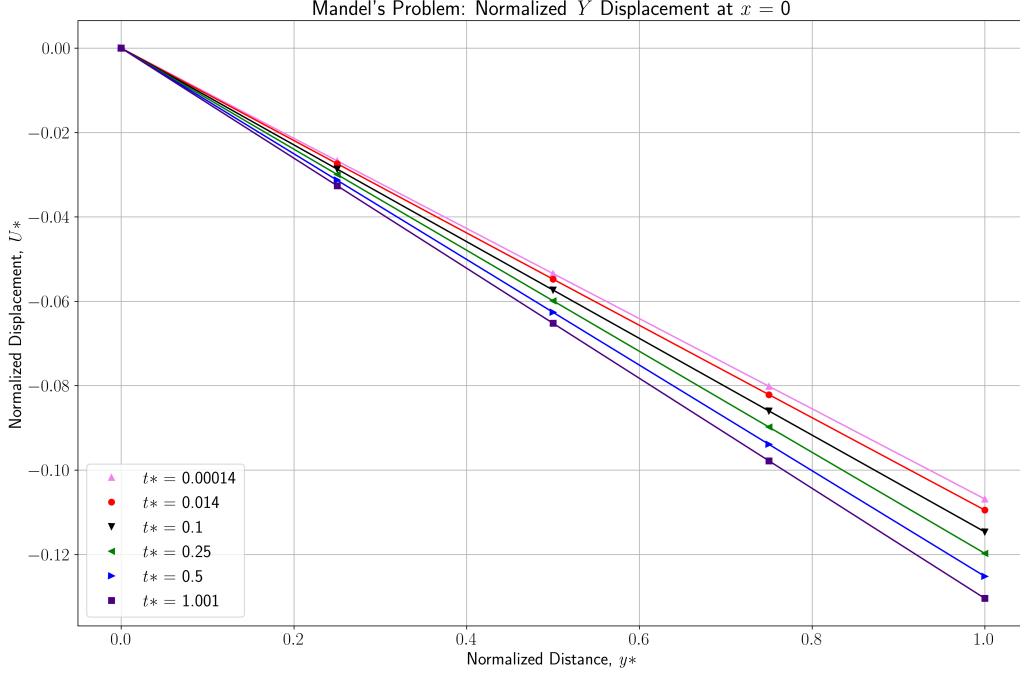


Figure 13: Displacement along the y axis at $x = 0$, where displacement in the x direction is fixed a zero. This is for a mesh consisting of quadrilateral elements. We consider compressive displacement as negative, and define normalized displacement $U^* = \frac{U_y}{b}$, with b referring to the vertical (y axis) thickness of the quarter domain. Numerically generated normalized displacement is represented by continuous lines with shapes representing analytical solutions at discrete points overlain. The shapes representing analytical solutions are varied with regard to the normalized time that they represent. These values are plotted over a normalized distance over the y axis $y^* = \frac{y}{b}$. Results are plotted for distinct snapshots of normalized time $t^* = \frac{ct}{a^2}$, where a represents the length of the quarter domain along the x axis, and the consolidation coefficient, c , defined in Appendix A2. We observe consolidation that agrees well with our analytical solution.

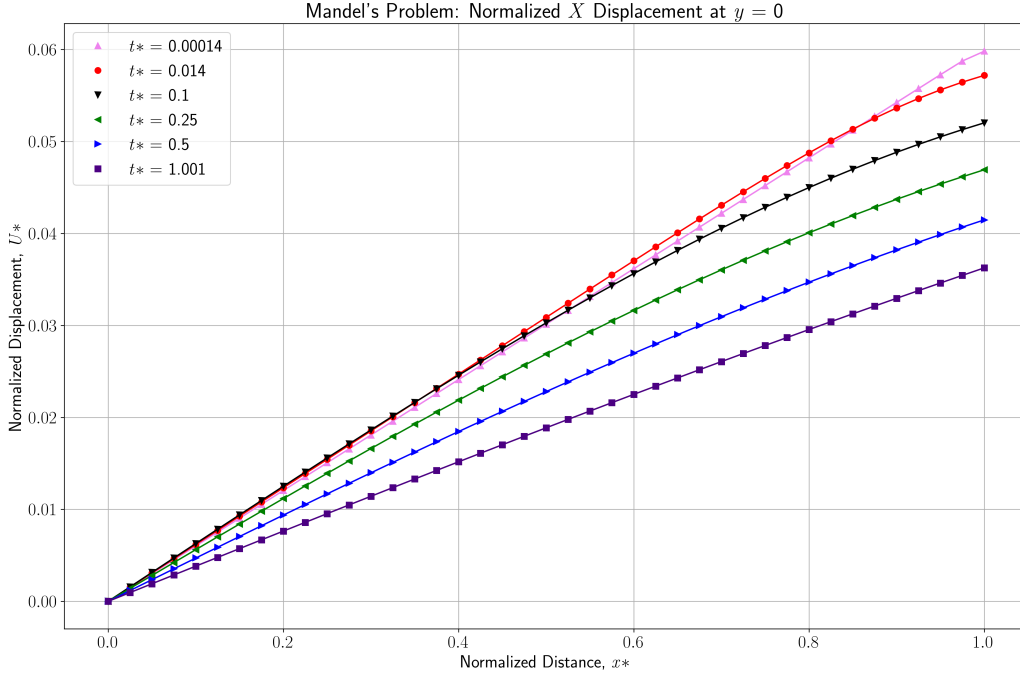


Figure 14: Displacement in the x direction along a line drawn at $y = 0$ for a mesh consisting of quadrilateral elements.. We denote extensional displacement (positive with respect to the x axis) as positive. Normalized displacement is defined as $U^* = \frac{U_x}{a}$, with a referring to the horizontal (x axis) thickness of the quarter domain. Numerically generated normalized displacement is represented by continuous lines with shapes representing analytical solutions at discrete points overlain. The shapes representing analytical solutions are varied with regard to the normalized time that they represent. These values are plotted over a normalized distance over the x axis $x^* = \frac{x}{a}$. Results are plotted for distinct snapshots of normalized time $t^* = \frac{ct}{a^2}$, where the consolidation coefficient, c , defined in Appendix A2. The influence of the "Mandel-Cryer" effect is demonstrated in early time as a small increase in displacement attributable to a compaction induced increase in pressure. As the domain drains, and the pressure subsides, displacement recedes.

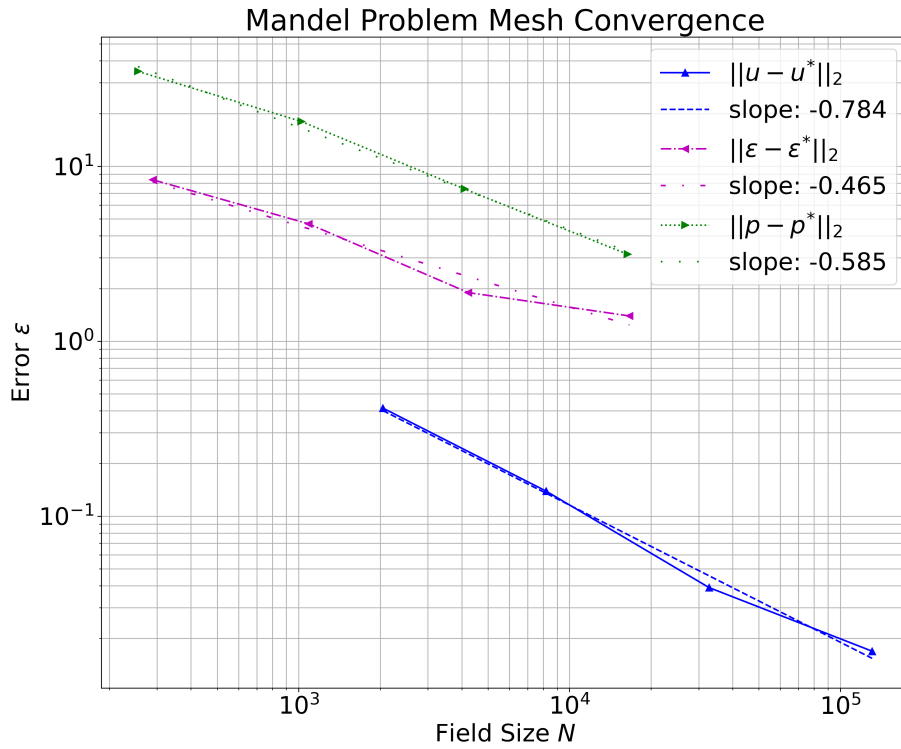


Figure 15: Mesh convergence is shown for Mandel’s problem. We consider convergence for displacement, u , volumetric strain, ϵ , and pressure, p . We do not quite achieve second-order convergence in the displacement, which we attribute to inaccuracy caused by the impulsive start.

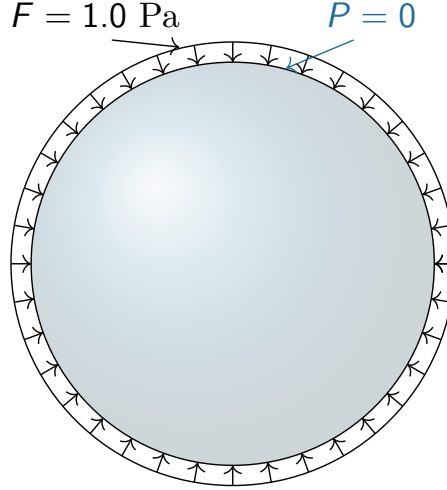


Figure 16: Diagram of Cryer's full problem. The problem consists of a saturated porous sphere subject to radial compressive stress. The surface boundary is considered to be permeable and maintained at ambient pressure conditions, allowing for free fluid outflow.

546 4.3 Poroelasticity and Fault Slip

547 In this example we combine the poroelasticity material with the existing fault for-
 548 mulation in PyLith (see Appendix Appendix G) to extend an example of two-dimensional
 549 strike-slip faulting. This demonstrates the modular PyLith design that allows the gen-
 550 eral fault formulation to be used with the new poroelasticity material formulation. We
 551 draw from the existing two-dimensional strike-slip example `examples/strikeslip-2d`
 552 in the PyLith source (Aagaard, Knepley, & Williams, 2022a) and change the material
 553 properties of the bulk from linear elastic to linear poroelastic. The model corresponds
 554 to a two-dimensional horizontal cross-section of a vertical strike-slip fault, with a length
 555 of 150 kilometers in the y direction and 100 kilometers in the x direction.

556 On each side of the fault we replace the elastic material and isotropic, linear elas-
 557 tic bulk rheology with a poroelastic material and isotropic, linear poroelastic bulk rhe-
 558 ology. The fault is modeled in the standard method for PyLith (Aagaard, Knepley, Williams,
 559 & Walker, 2022) and does not consider pore pressure, so that pore flux is continuous across
 560 the fault. Pore fluid pressure begins at zero and we discount gravitational body forces.
 561 We fix the x and y displacements on the $-x$ and $+x$ boundaries and prescribed 2.0 m
 562 of right-lateral slip as shown in Fig. 20. We assign material properties roughly approx-
 563 imating water filled sandstone, and the pressure field displays a pattern of compression

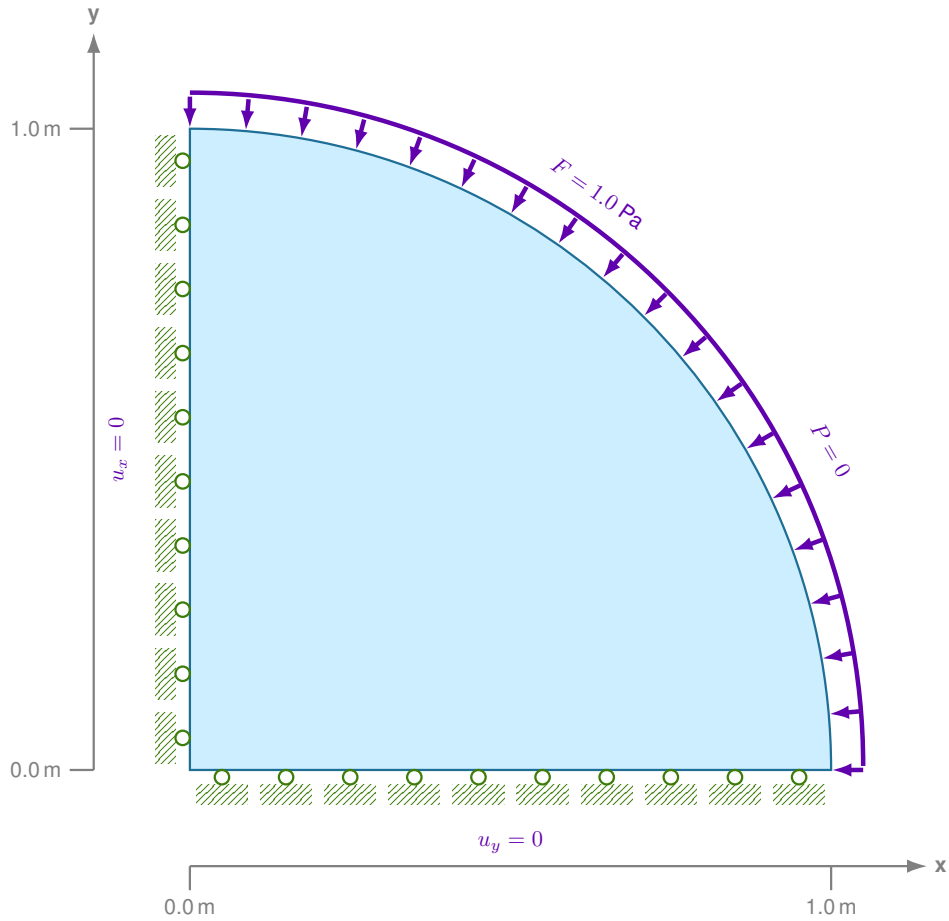


Figure 17: Owing to the symmetry of Cryer’s problem, we consider an eighth domain section. For simplicity we draw this domain in two-dimensions. The flat boundary faces do not permit displacement with respect to their respective directions. Similarly the surface facing out of plain toward the reader may be considered to be fixed with respect to the z axis. Radial compressive stress is applied over the curved, exterior boundary surface.

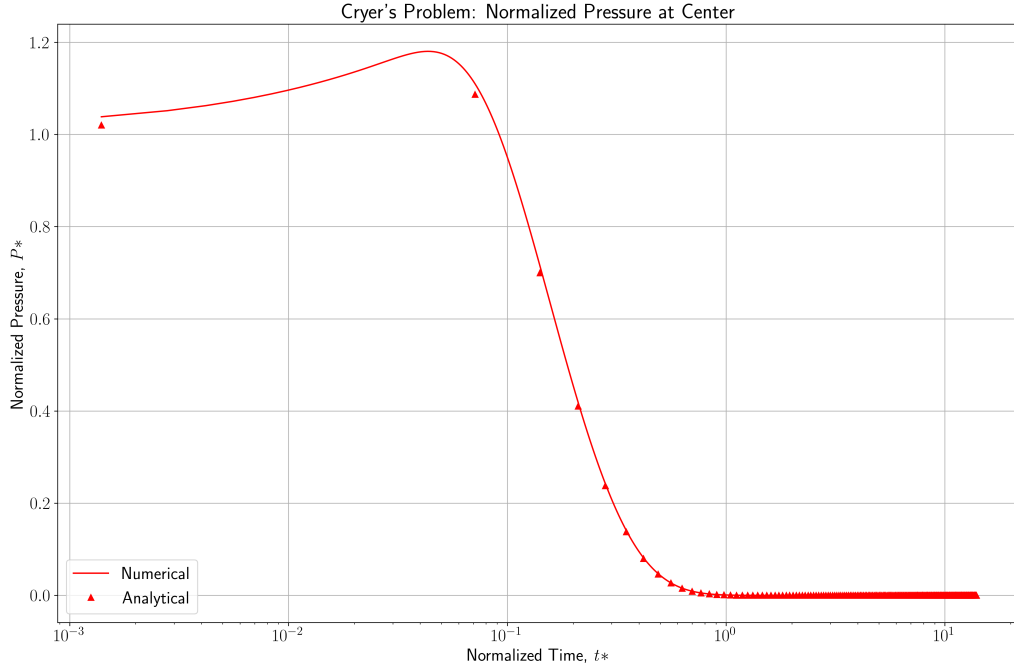


Figure 18: Normalized pressure at the origin of the eighth domain Cryer problem benchmark, using hexahedral mesh elements. We define normalized pressure $p^* = \frac{p}{F}$, where F is radial compressive stress on the domain. We plot numerical solutions for normalized pressure as a continuous line with analytical solutions plotted as triangles at discrete points in time. Both are plotted against a logarithmic representation of normalized time $t^* = \frac{ct}{R^2}$, where R refers to the radius of the spherical domain and the consolidation coefficient, c , is defined in Appendix A2. In both the numerical and analytical results, we observe an initial increase in pressure followed by a fall off to a drained condition.

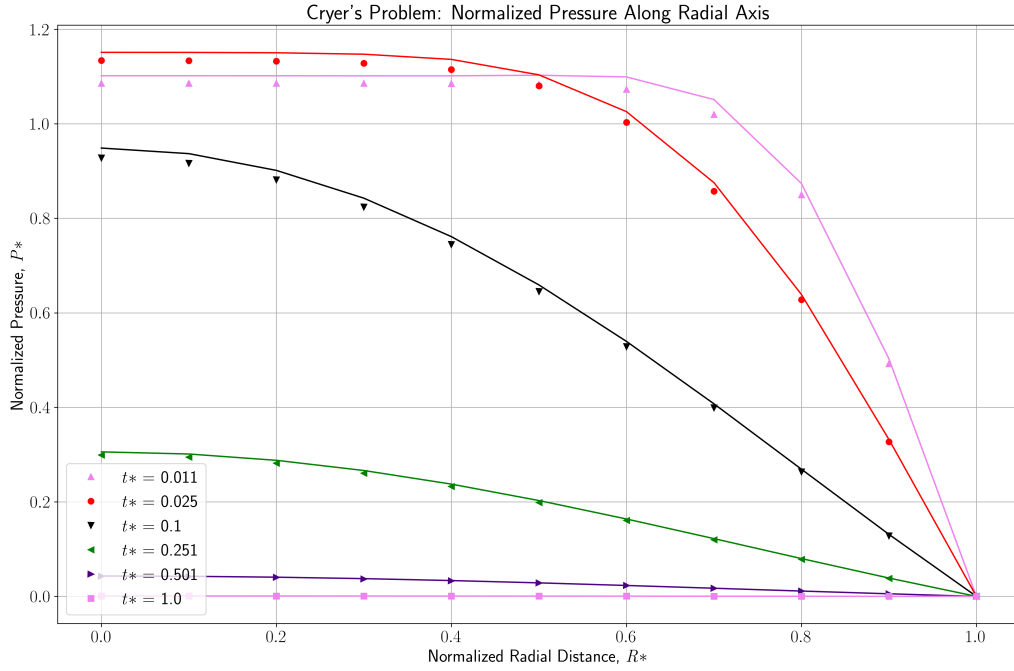


Figure 19: Normalized pressure along the radial axis the eighth domain Cryer problem Benchmark, using hexahedral mesh elements. We define normalized pressure $p^* = \frac{p}{F}$, where F is radial compressive stress on the domain. We plot normalized pressure profiles along a normalized radial distance $R^* = \frac{r}{R}$, where R refers to the radius of the spherical domain. Profiles are plotted for specific points in normalized time $t^* = \frac{ct}{R^2}$. Both numerical and analytical solutions display non-monotonic pressure behavior in early time and decay toward drained conditions. Numerical solutions are represented by continuous lines with shapes representing analytical solutions. The shapes representing analytical solutions are varied with regard to the normalized time that they represent.

564 and rarefaction. This resultant pressure profile is indicative of a system where shear along
 565 the fault is the only input force. Compared side by side with the original example which
 566 uses a linear elastic material, the elastic material has higher stress concentration and larger
 567 gradients near the fault boundaries. In Fig. 21 the left and right boundaries are fixed
 568 with respect to the x axis. The fault slip produces a torque and pressure takes extreme
 569 values at the corners of the domain.

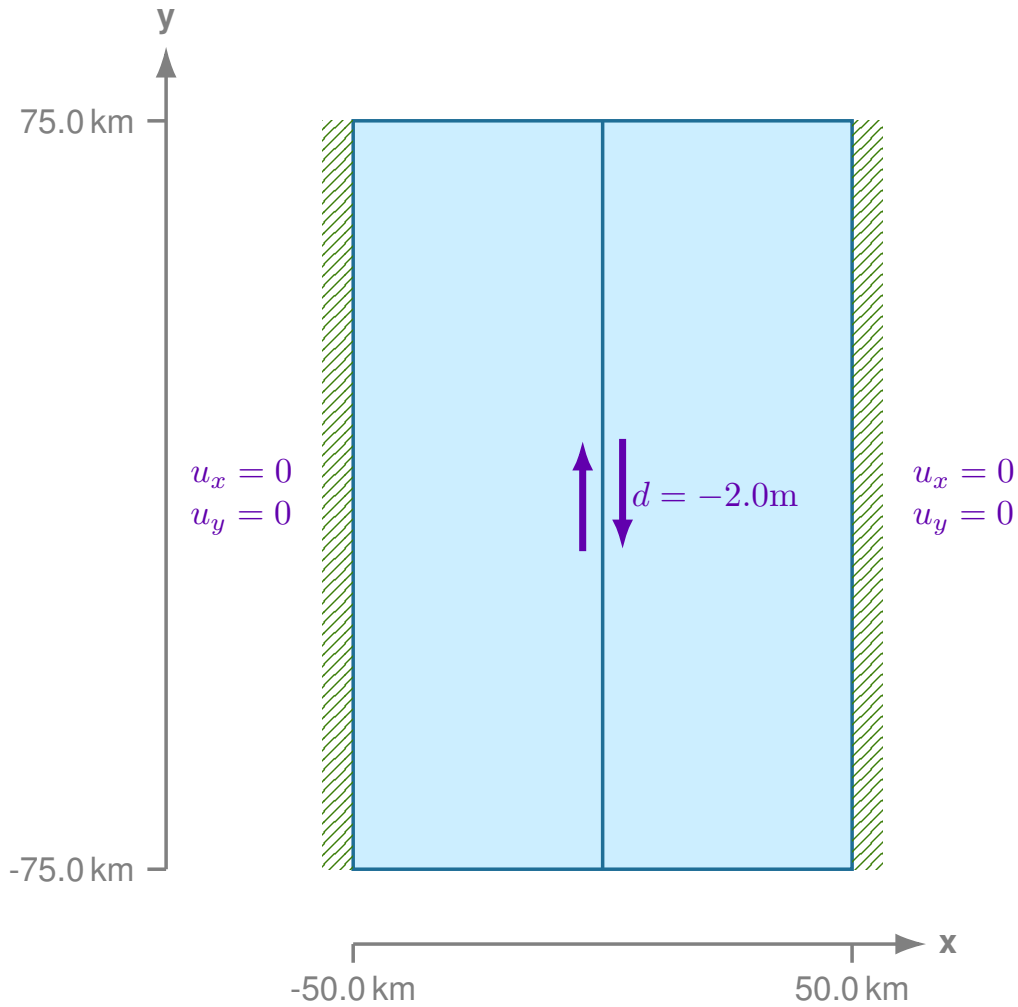


Figure 20: Diagram of the domain for the strike-slip example problem. We represent a vertical strike slip fault with 2.0 m of prescribed right-lateral slip. We fix the boundaries at the x axis edges with respect to both components of displacement.

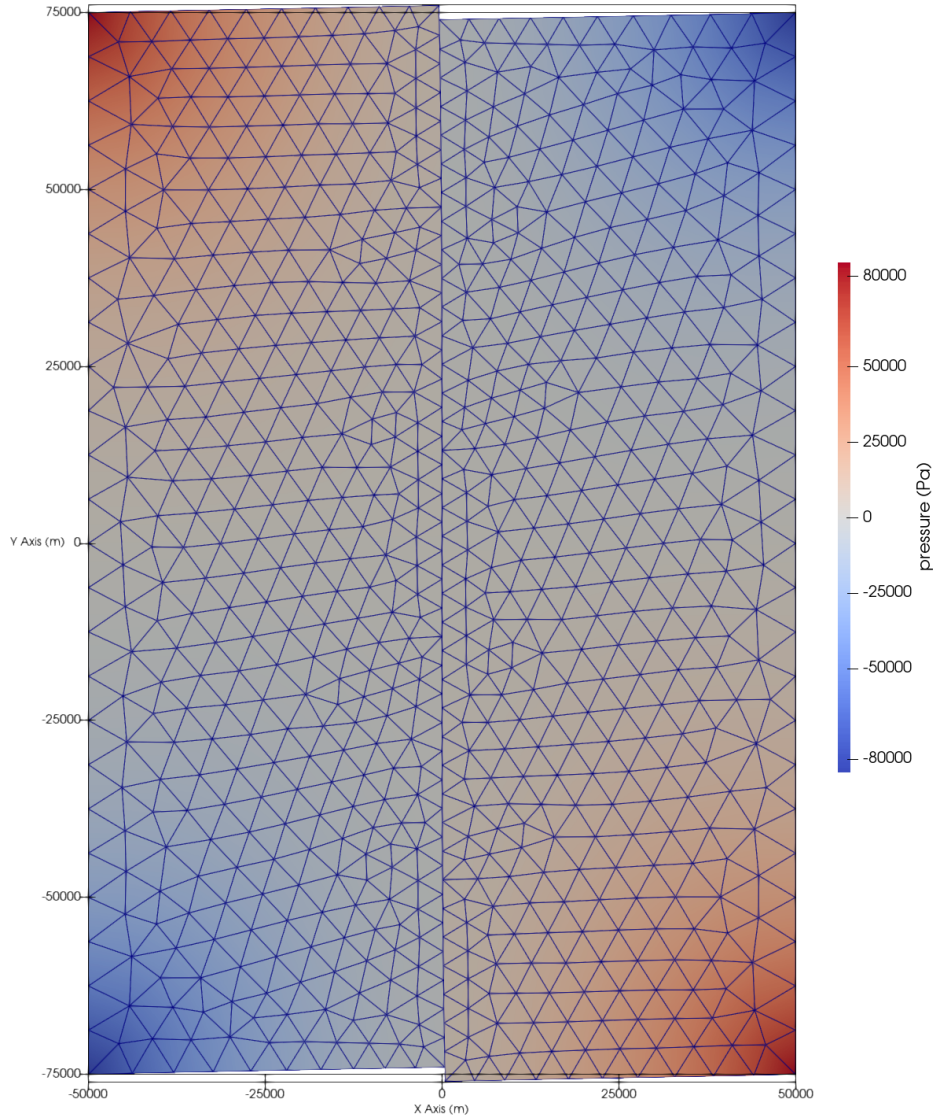


Figure 21: Pressure results for the prescribed strike-slip example combined with a poroelastic material. We apply 2.0 m of right-lateral slip along the fault bisecting the domain. We observe a pattern of poroelastic compression and rarefaction in line with our prescribed displacement.

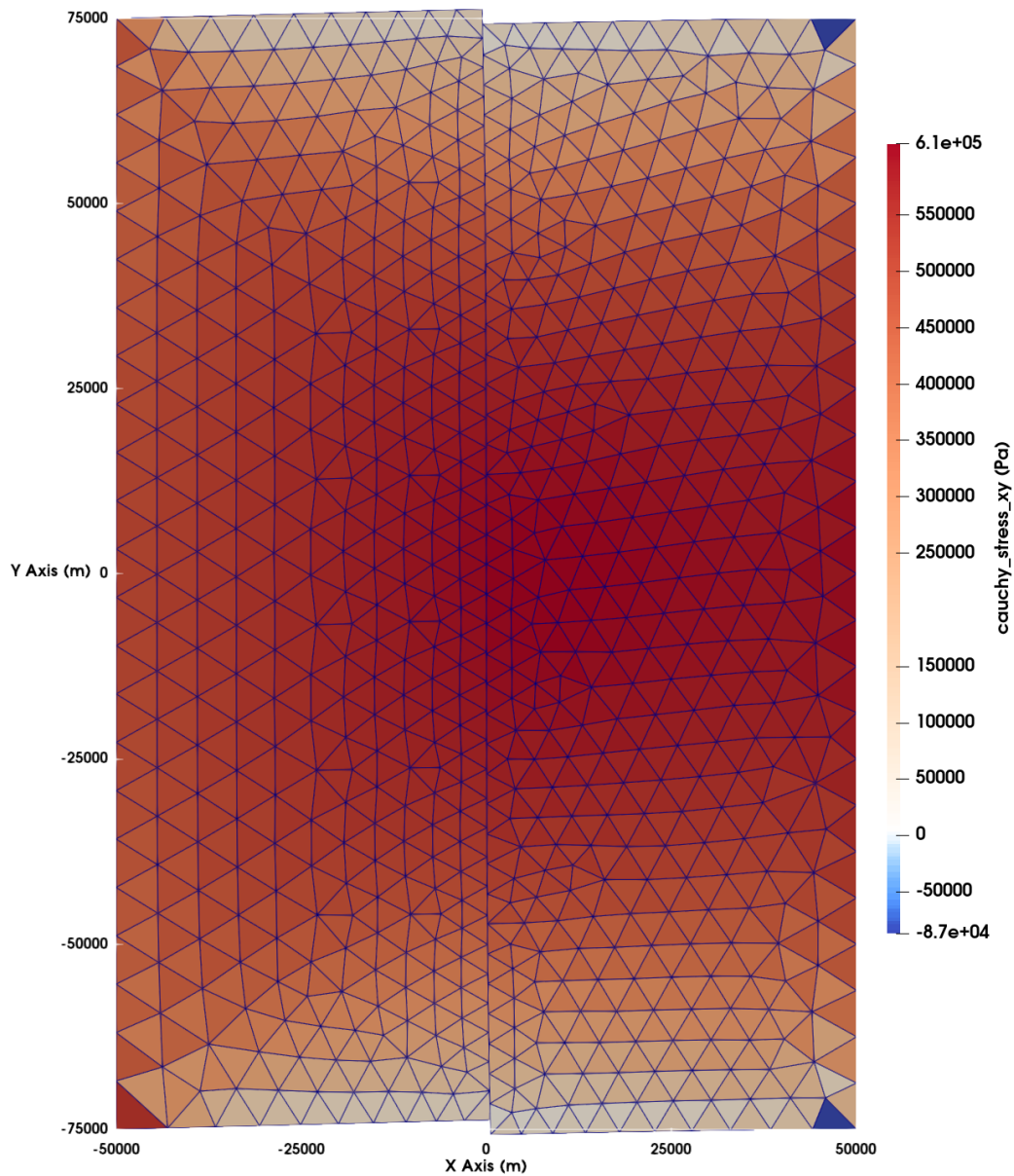


Figure 22: Cauchy stress for the prescribed strike-slip example, to which we apply 2.0 m of right-lateral slip along the fault bisecting the domain. Here we show a linear elastic material, in comparison to the linear poroelastic material in Fig. 23, and we see that the elastic material has much higher stress concentration near the fault.

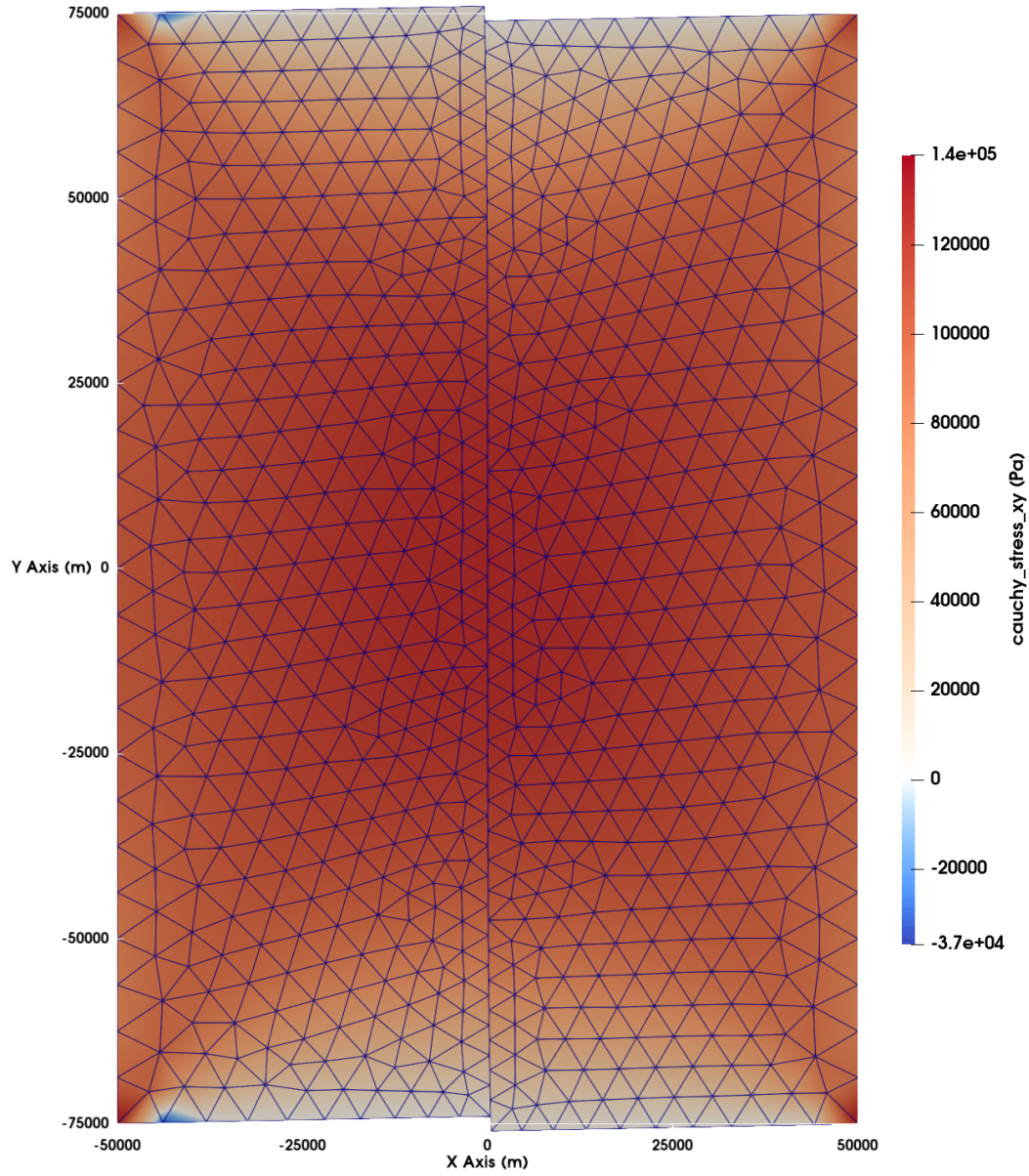


Figure 23: Cauchy stress for the prescribed strike-slip example, to which we apply 2.0 m of right-lateral slip along the fault bisecting the domain. We show a linear poroelastic material, in comparison to the linear elastic material in Fig. 22, and we see that the elastic material has much higher stress concentration near the fault.

570 **5 Conclusion**

571 We demonstrated the new multiphysics infrastructure in PyLith by incorporating
 572 fluid flow through porous media into the existing solid mechanics. Our fully coupled ap-
 573 proach solves for both fluid pressure and displacement simultaneously. Because our model
 574 is fully coupled, it does not produce the spurious solutions possible with operator split-
 575 ting approaches. We verified the poroelastic implementation using both the Method of
 576 Manufactured Solutions and full-scale test problems with analytical solutions. The ver-
 577 ification tests illustrate the robustness and fidelity of the formulation. Additionally, we
 578 combined the new poroelastic material model with the existing fault formulation in PyLith.
 579 Future work could expand the fault formulation to incorporate poroelastic behavior within
 580 the fault itself. This would involve steps similar to adding the bulk poroelastic model,
 581 such as incorporating additional solution fields and physical coupling.

582 **Acknowledgments**

583 We gratefully acknowledge funding from the National Science Foundation Computational
 584 Infrastructure for Geodynamics project, NSF EAR-094944. In addition, this work was
 585 partially funded by grant NSF CSSI: 1931524, as well as through the Department of En-
 586 ergy Applied Math Research division, U.S. DOE Contract DE-AC02-06CH11357. Any
 587 use of trade, firm, or product names is for descriptive purposes only and does not im-
 588 ply endorsement by the U.S. Government.

589 **Data Availability Statement**

590 The PyLith v3.0.3 source code, which includes the input files for the full-scale tests, are
 591 available in (Aagaard, Knepley, & Williams, 2022a), at <https://doi.org/10.5281/zenodo.7072811>.

592 **References**

- 593 Aagaard, B., Knepley, M., & Williams, C. (2013). A domain decomposition ap-
 594 proach to implementing fault slip in finite-element models of quasi-static and
 595 dynamic crustal deformation. *Journal of Geophysical Research: Solid Earth*,
 596 *118*, 3059-3079. doi: 10.1002/jgrb.50217
- 597 Aagaard, B., Knepley, M., & Williams, C. (2022a). *geodynamics/pylith v3.0.2*. Zen-
 598 odo. Retrieved from <https://doi.org/10.5281/zenodo.6914592> doi: 10
 599 .5281/zenodo.6914592
- 600 Aagaard, B., Knepley, M. G., & Williams, C. (2022b, Sep). *geodynamics/pylith*
 601 *v3.0.3*. Zenodo. doi: 10.5281/zenodo.598181
- 602 Aagaard, B., Knepley, M. G., & Williams, C. (2023). *PyLith*. Retrieved from

- 603 <http://geodynamics.org/resources/pylith/>
- 604 Aagaard, B., Knepley, M. G., Williams, C., & Walker, R. (2022). *PyLith User Man-*
 605 *ual version 3.0.3*. Retrieved from <https://pylith.readthedocs.io/en/v3.0>
 606 [.3/](https://pylith.readthedocs.io/en/v3.0)
- 607 Aagaard, B., Williams, C., & Knepley, M. (2007). Pylith: A finite-element code for
 608 modeling quasi-static and dynamic crustal deformation. *Eos*, *88*(52), T21B–
 609 0592.
- 610 Abdelfattah, A., Barra, V., Beams, N., Brown, J., Camier, J.-S., Dobrev, V., . . . To-
 611 mov, S. (2021). *libCEED user manual*. Zenodo. doi: 10.5281/zenodo.5077489
- 612 Abousleiman, Y., Cheng, A. H., Cui, L., Detournay, E., & Roegiers, J. C. (1996).
 613 Mandel’s problem revisited. *Geotechnique*, *46*, 187-195. doi: 10.1680/
 614 geot.1996.46.2.187
- 615 Abramowitz, M., & Stegun, I. A. (1964). *Handbook of mathematical functions with*
 616 *formulas, graphs, and mathematical tables* (ninth Dover printing, tenth GPO
 617 printing ed.). New York: Dover.
- 618 Balay, S., Abhyankar, S., Adams, M. F., Benson, S., Brown, J., Brune, P., . . .
 619 Zhang, J. (2023a). *PETSc/TAO users manual* (Tech. Rep. No. ANL-21/39 -
 620 Revision 3.19). Argonne National Laboratory. doi: 10.2172/1968587
- 621 Balay, S., Abhyankar, S., Adams, M. F., Benson, S., Brown, J., Brune, P., . . .
 622 Zhang, J. (2023b). *PETSc Web page*. <https://petsc.org/>. Retrieved
 623 from <https://petsc.org/>
- 624 Bangerth, W., Hartmann, R., & Kanschat, G. (2007). deal.II – a general purpose
 625 object oriented finite element library. *ACM Transactions on Mathematical*
 626 *Software*, *33*(4), 24/1–24/27.
- 627 Barros, L. D., Cappa, F., Guglielmi, Y., Duboeuf, L., & Grasso, J. R. (2019). En-
 628 ergy of injection-induced seismicity predicted from in-situ experiments. *Scien-*
 629 *tific Reports*, *9*(1), 4999. doi: 10.1038/s41598-019-41306-x
- 630 Bear, J. (1972). *Dynamics of fluids in porous media*. Dover Publications.
- 631 Béreux, F. (1996). Zero-relaxation limit versus operator splitting for two-phase fluid
 632 flow computations. *Computer Methods in Applied Mechanics and Engineering*,
 633 *133*(1-2), 93–124.
- 634 Biot, M. A. (1941). General theory of three-dimensional consolidation. *Journal of*
 635 *Applied Physics*, *12*, 155-164. doi: 10.1063/1.1712886
- 636 Biot, M. A. (1955). Theory of elasticity and consolidation for a porous anisotropic
 637 solid. *Journal of Applied Physics*, *26*, 182-185. doi: 10.1063/1.1721956
- 638 Biot, M. A. (1956a). General solutions of the equations of elasticity and consolida-
 639 tion for a porous material. *Journal of Applied Mechanics*, *23*(1), 91–96. doi:

640 10.1115/1.4011213

641 Biot, M. A. (1956b). Theory of deformation of a porous viscoelastic anisotropic
642 solid. *Journal of Applied Physics*, *27*, 459–467. doi: 10.1063/1.1722402

643 Biot, M. A. (1956c). Theory of propagation of elastic waves in a fluid-saturated
644 porous solid ii. higher frequency range. *Journal of the Acoustical Society of
645 America*, *28*, 179–191. doi: 10.1121/1.1908241

646 Boley, B. (1974). Thermal stresses today (developments in solids and structural
647 elements). In *U.S. National Congress of Applied Mechanics, 7th* (pp. 99–107).
648 Boulder, CO.

649 Boley, B., & Weiner, J. (2012). *Theory of thermal stresses*. Dover Publications.

650 Bostock, J., & Riley, H. T. (2011). *The natural history of Pliny* (Vol. 4). London: H.
651 G. Bohn. (Translation of *Naturalis historia*) doi: 10.5962/bhl.title.8126

652 Brooks, A. N., & Hughes, T. J. (1982). Streamline upwind/Petrov-Galerkin for-
653 mulations for convection dominated flows with particular emphasis on the
654 incompressible Navier-Stokes equations. *Computer Methods in Applied Me-
655 chanics and Engineering*, *32*(1-3), 199–259.

656 Brown, J., Abdelfattah, A., Barra, V., Beams, N., Camier, J. S., Dobrev, V.,
657 ... Tomov, S. (2021). libCEED: Fast algebra for high-order element-
658 based discretizations. *Journal of Open Source Software*, *6*(63), 2945. doi:
659 10.21105/joss.02945

660 Brown, J., Knepley, M. G., May, D. A., McInnes, L. C., & Smith, B. F. (2012).
661 Composable linear solvers for multiphysics. In *Proceedings of the 11th In-
662 ternational Symposium on Parallel and Distributed Computing (ISPDC 2012)*
663 (pp. 55–62). IEEE Computer Society. doi: 10.1109/ISPDC.2012.16

664 Brown, J., Knepley, M. G., & Smith, B. (2015, Jan). Run-time extensibility and li-
665 brarization of simulation software. *IEEE Computing in Science and Engineer-
666 ing*, *17*(1), 38–45. doi: 10.1109/MCSE.2014.95

667 Brune, P. R., Knepley, M. G., Smith, B. F., & Tu, X. (2015). Composing scal-
668 able nonlinear algebraic solvers. *SIAM Review*, *57*(4), 535–565. doi: 10.1137/
669 130936725

670 Cacace, M., Hofmann, H., & Shapiro, S. A. (2021, December). Projecting seis-
671 micity induced by complex alterations of underground stresses with ap-
672 plications to geothermal systems. *Scientific Reports*, *11*(1), 23560. doi:
673 10.1038/s41598-021-02857-0

674 Cacace, M., & Jacquy, A. B. (2017). Flexible parallel implicit modelling of cou-
675 pled thermal–hydraulic–mechanical processes in fractured rocks. *Solid Earth*,
676 *8*, 921–941. doi: 10.5194/se-8-921-2017

- 677 Carman, P. G. (1997). Fluid flow through granular beds. *Chemical Engineering Re-*
678 *search and Design*, 75(1 SUPPL.), S32–S48. doi: 10.1016/s0263-8762(97)80003
679 -2
- 680 Cheng, A. (2016). *Poroelasticity*. Springer International Publishing. doi: 10.1007/
681 978-3-319-25202-5
- 682 Cheng, A., Zhou, P., Yan, B., Wang, Y., & Killough, J. (2017). Adaptive time
683 stepping with the modified local error method for coupled flow-geomechanics
684 modeling. *Society of Petroleum Engineers - SPE Reservoir Characterisa-*
685 *tion and Simulation Conference and Exhibition, RCSC 2017*, 296-309. doi:
686 10.2118/186030-ms
- 687 Ciarlet, P. G. (1976). *Numerical analysis of the finite element method* (Vol. 59).
688 Presses de l'Université de Montréal.
- 689 Coussy, O. (2005). *Poromechanics*. John Wiley and Sons. doi: 10.1002/0470092718
- 690 Craft, B. C., Hawkins, M. F., & Terry, R. E. (1991). *Applied Petroleum Reservoir*
691 *Engineering*. Prentice Hall.
- 692 Cryer, C. W. (1963). A comparison of the three-dimensional consolidation theories
693 of Biot and Terzaghi. *Quarterly Journal of Mechanics and Applied Mathemat-*
694 *ics*, 16, 401-412. doi: 10.1093/qjmam/16.4.401
- 695 da Vinci, L. (2019). The Codex Leicester. In D. Laurenza & M. Kemp (Eds.),
696 *Leonardo da Vinci's Codex Leicester: A New Edition* (Vol. 3: Transcrip-
697 tion and Translation). Oxford University Press. doi: 10.1093/oseo/
698 instance.00265758
- 699 Dean, R., Xiuli, G., Stone, C., & Minkoff, S. (2003). A comparison of techniques for
700 coupling porous flow and geomechanics. In *SPE Reservoir Simulation Sympo-*
701 *sium*. doi: 10.2118/79709-PA
- 702 Dean, R. H., Gai, X., Stone, C. M., & Minkoff, S. E. (2006). A comparison of tech-
703 niques for coupling porous flow and geomechanics. *SPE Journal*, 11, 132-140.
704 doi: 10.2118/79709-PA
- 705 Dusseault, M. (2008). Coupling geomechanics and transport in petroleum engineer-
706 ing. In *SHIRMS 2008: Proceedings of the First Southern Hemisphere Interna-*
707 *tional Rock Mechanics Symposium*. doi: 10.36487/acg_repo/808_44
- 708 Ellsworth, W. L. (2013). Injection-induced earthquakes. *Science*, 341, 142-149. doi:
709 10.1126/science.1225942
- 710 Gaston, D., Newman, C., Hansen, G., & Lebrun-Grandié, D. (2009). MOOSE: A
711 parallel computational framework for coupled systems of nonlinear equations.
712 *Nuclear Engineering and Design*, 239(10), 1768–1778.
- 713 Goebel, T., Weingarten, M., Chen, X., Haffener, J., & Brodsky, E. E. (2017). The

- 714 2016 Mw5.1 Fairview, Oklahoma earthquakes: Evidence for long-range poroe-
715 lastic triggering at > 40 km from fluid disposal wells. *Earth and Planetary*
716 *Science Letters*, *472*, 50-61. doi: 10.1016/j.epsl.2017.05.011
- 717 Gurevich, A. E., & Chilingarian, G. V. (1995). Possible impact of subsidence on gas
718 leakage to the surface from subsurface oil and gas reservoirs. *Developments in*
719 *Petroleum Science*, *41*, 193-213. doi: 10.1016/S0376-7361(06)80051-8
- 720 Ham, D. A., & Team, F. (2022). *The Firedrake project*. Retrieved from [http://](http://firedrakeproject.org)
721 firedrakeproject.org
- 722 Healy, J. H., Rubey, W. W., Griggs, D. T., & Raleigh, C. B. (1968). *The Denver*
723 *earthquakes* (Vol. 161). doi: 10.1126/science.161.3848.1301
- 724 Hough, S. E., & Bilham, R. (2018). Revisiting earthquakes in the Los Angeles,
725 California basin during the early instrumental period: Evidence for an associ-
726 ation with oil production. *Journal of Geophysical Research: Solid Earth*, *123*,
727 10,684-10,705. doi: 10.1029/2017JB014616
- 728 Hough, S. E., & Page, M. (2016). Potentially induced earthquakes during the early
729 twentieth century in the Los Angeles basin. *Bulletin of the Seismological Soci-*
730 *ety of America*, *106*, 2419-2435. doi: 10.1785/0120160157
- 731 Hutka, G. A., Cacace, M., Hofmann, H., Zang, A., Wang, L., & Ji, Y. (2023). Nu-
732 merical investigation of the effect of fluid pressurization rate on laboratory-
733 scale injection-induced fault slip. *Scientific Reports*, *13*(1), 4437. doi:
734 10.1038/s41598-023-30866-8
- 735 Isaac, T., & Knepley, M. G. (2017). Support for non-conformal meshes in PETSc's
736 DMPlex interface. *ACM Transactions on Mathematical Software*.
- 737 Jha, B., & Juanes, R. (2007). A locally conservative finite element framework for
738 the simulation of coupled flow and reservoir geomechanics. *Acta Geotechnica*,
739 *2*, 139-153. doi: 10.1007/s11440-007-0033-0
- 740 Jha, B., & Juanes, R. (2014). Coupled multiphase flow and poromechanics: A com-
741 putational model of pore pressure effects on fault slip and earthquake trigger-
742 ing. *Water Resources Research*, *50*, 3776-3808. doi: 10.1002/2013WR015175
- 743 Kim, J., Tchelepi, H. A., & Juanes, R. (2011a). Stability and convergence of sequen-
744 tial methods for coupled flow and geomechanics: Drained and undrained splits.
745 *Computer Methods in Applied Mechanics and Engineering*, *200*, 2094-2116.
746 doi: 10.1016/j.cma.2011.02.011
- 747 Kim, J., Tchelepi, H. A., & Juanes, R. (2011b). Stability and convergence of sequen-
748 tial methods for coupled flow and geomechanics: Fixed-stress and fixed-strain
749 splits. *Computer Methods in Applied Mechanics and Engineering*, *200*(13-16),
750 1591-1606. doi: 10.1016/j.cma.2010.12.022

- 751 Kirby, R. C. (2004). Algorithm 839: FIAT, a new paradigm for computing finite
 752 element basis functions. *ACM Transactions on Mathematical Software*, 30(4),
 753 502–516. doi: 10.1145/1039813.1039820
- 754 Klöckner, A. (2014). Loo.py: transformation-based code generation for GPUs and
 755 CPUs. In *Proceedings of ACM SIGPLAN International Workshop on Li-*
 756 *braries, Languages, and Compilers for Array Programming* (pp. 82–87). doi:
 757 10.1145/2627373.2627387
- 758 Knepley, M. G., Brown, J., Rupp, K., & Smith, B. F. (2013, September). Achieving
 759 high performance with unified residual evaluation. *ArXiv e-prints*. Retrieved
 760 from <http://adsabs.harvard.edu/abs/2013arXiv1309.1204K>
- 761 Knepley, M. G., & Karpeev, D. A. (2009). Mesh algorithms for PDE with Sieve I:
 762 Mesh distribution. *Scientific Programming*, 17(3), 215–230. Retrieved from
 763 <http://arxiv.org/abs/0908.4427> doi: 10.3233/SPR-2009-0249
- 764 Knepley, M. G., Lange, M., & Gorman, G. J. (2017). *Unstructured overlapping mesh*
 765 *distribution in parallel*. doi: 10.48550/arXiv.1506.06194
- 766 Knut-Andreas Lie, O. M. (Ed.). (2021). *Advanced modeling with the MAT-*
 767 *LAB reservoir simulation toolbox*. Cambridge University Press. doi:
 768 10.1017/9781009019781
- 769 Krogstad, S., Lie, K., Møyner, O., Møll Nilsen, H., Raynaud, X., and Skaflestad, &
 770 Ict, S. (2015). SPE 173317-MS MRST-AD – an Open-Source Framework for
 771 Rapid Prototyping and Evaluation of Reservoir Simulation Problems. *SPE*
 772 *Reservoir Simulation Symposium*, 23–25. doi: SPE-173317-MS
- 773 Lange, M., Mitchell, L., Knepley, M. G., & Gorman, G. J. (2016). Efficient mesh
 774 management in Firedrake using PETSc-DMPlex. *SIAM Journal on Scientific*
 775 *Computing*, 38(5), S143–S155. doi: 10.1137/15M1026092
- 776 Lie, K.-A. (2019). *An introduction to reservoir simulation using MATLAB/GNU*
 777 *Octave: User guide for the MATLAB Reservoir Simulation Toolbox (MRST)*.
 778 Cambridge University Press. doi: 10.1017/9781108591416
- 779 Lindsay, A. D., Gaston, D. R., Permann, C. J., Miller, J. M., Andrš, D., Slaughter,
 780 A. E., ... Wong, C. (2022). 2.0 - MOOSE: Enabling massively parallel multi-
 781 physics simulation. *SoftwareX*, 20, 101202. doi: 10.1016/j.softx.2022.101202
- 782 Logg, A., Mardal, K.-A., & Wells, G. (Eds.). (2012). *Automated solution of dif-*
 783 *ferential equations by the finite element method: The fenics book* (Vol. 84).
 784 Springer.
- 785 Logg, A., Ølgaard, K., Rognes, M., Wells, G., Jansson, J., Kirby, R., ... Skavhaug,
 786 O. (2011). *The FEniCS project*. Retrieved from <http://fenicsproject.org>
- 787 Mandel, J. (1953). Consolidation des sols (étude mathématique). *Geotechnique*, 3,

- 788 287-299. doi: 10.1680/geot.1953.3.7.287
- 789 Mardal, K.-A., Rognes, M. E., & Thompson, T. B. (2021). Accurate discretization
790 of poroelasticity without Darcy stability – Stokes-Biot stability revisited. *BIT*
791 *Numerical Mathematics*, 1–36.
- 792 May, D. A., & Moresi, L. (2008). Preconditioned iterative methods for Stokes flow
793 problems arising in computational geodynamics. *Physics of the Earth and*
794 *Planetary Interiors*, 171(1-4), 33–47. doi: 10.1016/j.pepi.2008.07.036
- 795 McCormack, K., Hesse, M. A., Dixon, T., & Malservisi, R. (2020). Modeling the
796 contribution of poroelastic deformation to postseismic geodetic signals. *Geo-*
797 *physical Research Letters*, 47(8), 1–10. doi: 10.1029/2020GL086945
- 798 Median, D. N. (1994, aug). Rock mechanics issues in petroleum engineering. In *1st*
799 *North American Rock Mechanics Symposium, NARMS 1994* (Vol. All Days,
800 pp. 3–17).
- 801 Meng, C. (2017). Benchmarking Defmod, an open source fem code for modeling
802 episodic fault rupture. *Computers and Geosciences*, 100, 10-26. doi: 10.1016/
803 j.cageo.2016.11.014
- 804 Muir-Wood, R., & King, G. C. (1993). Hydrological signatures of earthquake strain.
805 *Journal of Geophysical Research*, 98, 22035. doi: 10.1029/93jb02219
- 806 Naumov, D. Y., Bilke, L., Fischer, T., Rink, K., Wang, W., Watanabe, N., ... Ning,
807 Z. (2022, 4). *OpenGeoSys*. Retrieved from <https://www.opengeosys.org>
808 doi: 10.5281/zenodo.6405711
- 809 Nur, A., & Booker, J. R. (1972). Aftershocks caused by pore fluid flow? *Science*,
810 175, 885-887. doi: 10.1126/science.175.4024.885
- 811 Oberkampf, W. L., Trucano, T. G., & Hirsch, C. (2004). Verification, validation,
812 and predictive capability in computational engineering and physics. *Applied*
813 *Mechanics Reviews*, 57, 345-384. doi: 10.1115/1.1767847
- 814 Odeh, A. S. (1982). An overview of mathematical modeling of the behavior of hydro-
815 carbon reservoirs. *SIAM Review*, 24(3), 263–273. doi: 10.1137/1024062
- 816 Peltzer, G., Rosen, P., Rogez, F., & Hudnut, K. (1998). Poroelastic rebound along
817 the Landers 1992 earthquake surface rupture. *Journal of Geophysical Research:*
818 *Solid Earth*, 103, 30131-30145. doi: 10.1029/98jb02302
- 819 Piersanti, E., Lee, J. J., Thompson, T., Mardal, K.-A., & Rognes, M. E. (2021).
820 Parameter robust preconditioning by congruence for multiple-network poroe-
821 lasticity. *SIAM Journal on Scientific Computing*, 43(4), B984–B1007.
- 822 Podgorney, R., Finnilla, A., Simmons, S., & McLennan, J. (2021). A reference
823 thermal-hydrologic-mechanical native state model of the Utah FORGE en-
824 hanced geothermal site. *Energies*, 14(16), 1–26. doi: 10.3390/en14164758

- 825 Poland, J. F., & Davis, G. H. (1969, 1). *Land subsidence due to withdrawal of fluids*
826 (Vol. 2). Geological Society of America. doi: 10.1130/REG2-p187
- 827 Pratt, W. E., & Johnson, D. W. (1926, 10). Local subsidence of the Goose Creek oil
828 field. *The Journal of Geology*, *34*, 577-590. doi: 10.1086/623352
- 829 Raleigh, C. B., Healy, J. H., & Bredenhoft, J. D. (1976). An experiment in earth-
830 quake control at Rangely, Colorado. *Science*, *191*, 1230-1237. doi: 10.1126/
831 science.191.4233.1230
- 832 Range, I. L.-F., & Biot, M. A. (1956). *Theory of propagation of elastic waves in a*
833 *fluid-saturated porous solid* (Vol. 28). Soc. of Expl. Geophys. (Reprinted from
834 J. Acoust. Soc. Am., 28, No. 2, 179-191) doi: 10.1121/1.1908239
- 835 Rathgeber, F., Ham, D. A., Mitchell, L., Lange, M., Luporini, F., McRae, A. T.,
836 ... Kelly, P. H. (2017). Firedrake: automating the finite element method
837 by composing abstractions. *ACM Transactions on Mathematical Software*,
838 *43*(24).
- 839 Rice, J. R., & Cleary, M. P. (1976). Some basic stress diffusion solutions for fluid-
840 saturated elastic porous media with compressible constituents. *Reviews of Geo-*
841 *physics*, *14*(2), 227-241. doi: 10.1029/RG014i002p00227
- 842 Roache, P. J. (2002). Code verification by the method of manufactured solutions.
843 *Journal of Fluids Engineering*, *124*(1), 4-10.
- 844 Ropp, D. L., & Shadid, J. N. (2009). Stability of operator splitting methods for sys-
845 tems with indefinite operators: Advection-diffusion-reaction systems. *Journal*
846 *of Computational Physics*, *228*(9), 3508-3516.
- 847 Rothenburg, L., & Bathurst, R. J. (1989). Analytical study of induced anisotropy in
848 idealized granular materials. *Geotechnique*, *39*(4), 601-614. doi: 10.1680/geot
849 .1989.39.4.601
- 850 Rowland, T. (n.d.). *Riesz representation theorem*. Retrieved from [https://](https://mathworld.wolfram.com/RieszRepresentationTheorem.html)
851 mathworld.wolfram.com/RieszRepresentationTheorem.html (Visited on
852 08/24/23)
- 853 Samier, P., Onaisi, A., & Fontaine, G. (2006). Comparisons of uncoupled and vari-
854 ous coupling techniques for practical field examples. *SPE Journal*, *11*, 89-102.
855 doi: 10.2118/79698-PA
- 856 Seeber, L., Armbruster, J. G., & Kim, W. Y. (2004). A fluid-injection-triggered
857 earthquake sequence in Ashtabula, Ohio: Implications for seismogenesis in sta-
858 ble continental regions. *Bulletin of the Seismological Society of America*, *94*,
859 76-87. doi: 10.1785/0120020091
- 860 Segall, P. (n.d.).

- 861 *Geology*, 942-946. doi: 10.1130/0091-7613(1989)017%3C0942:ETBFE%3E2.3
862 .CO;2
- 863 Segall, P. (2010). *Earthquake and volcano deformation*. Princeton University Press.
- 864 Segall, P., & Lu, S. (2015). Injection-induced seismicity: Poroelastic and earth-
865 quake nucleation effects. *Journal of Geophysical Research: Solid Earth*, 120,
866 5082-5103. doi: 10.1002/2015JB012060
- 867 Salvadurai, A. P. (2007). The analytical method in geomechanics. *Applied Mechanics*
868 *Reviews*, 60, 87-106. doi: 10.1115/1.2730845
- 869 Sibson, R. H. (1990). Rupture nucleation on unfavourably oriented faults. *Bulletin*
870 *- Seismological Society of America*, 80, 1580-1604. doi: 10.1016/0148-9062(92)
871 91063-b
- 872 Skempton, A. W. (1954). The pore-pressure coefficients a and b. *Geotechnique*, 4,
873 143-147. doi: 10.1680/geot.1954.4.4.143
- 874 Skoumal, R. J., Brudzinski, M. R., & Currie, B. S. (2015). Earthquakes induced
875 by hydraulic fracturing in Poland township, Ohio. *Bulletin of the Seismological*
876 *Society of America*, 105, 189-197. doi: 10.1785/0120140168
- 877 Stein, R. S. (1999). The role of stress transfer in earthquake occurrence. *Nature*,
878 402, 605-609. doi: 10.1038/45144
- 879 Tran, D., Settari, A., & Nghiem, L. (2004). New iterative coupling between a reser-
880 voir simulator and a geomechanics module. *SPE Journal*, 9, 362-369. doi: 10
881 .2118/88989-PA
- 882 von Terzaghi, K. (1923). Die Berechnung der Durchlässigkeit des Tones aus dem
883 Verlauf der hydromechanischen Spannungserscheinungen. *Sitzungsberichte der*
884 *Akademie der Wissenschaften in Wien, Mathematisch-Naturwissenschaftliche*
885 *Klasse*, 132, 125-138.
- 886 Wallwork, J. G., Knepley, M. G., Barral, N., & Piggott, M. D. (2022, January).
887 Parallel metric-based mesh adaptation in PETSc using ParMmg. In T. Robin-
888 son (Ed.), *Siam international meshing roundtable workshop 2022* (pp. 1–
889 5). Seattle, WA. Retrieved from [http://imr.sandia.gov/papers/imr31/
890 2026_imr31RJ.Wallwork.pdf](http://imr.sandia.gov/papers/imr31/2026_imr31RJ.Wallwork.pdf)
- 891 Wang, Z., & Liu, J. (2020). Deal.II implementation of a two-field finite element
892 solver for poroelasticity. In *International Conference on Computational Science*
893 (pp. 88–101). doi: 10.1007%2F978-3-030-50436-6_7
- 894 Xia, Y., Podgorney, R., & Huang, H. (2017). Assessment of a Hybrid Continu-
895 ous/Discontinuous Galerkin Finite Element Code for Geothermal Reservoir
896 Simulations. *Rock Mechanics and Rock Engineering*, 50(3), 719–732. doi:
897 10.1007/s00603-016-0951-y

898 Zhang, Y., Person, M., Rupp, J., Ellett, K., Celia, M. A., Gable, C. W., ... others
 899 (2013). Hydrogeologic controls on induced seismicity in crystalline basement
 900 rocks due to fluid injection into basal reservoirs. *Groundwater*, 51(4), 525–538.
 901 doi: 10.1111/gwat.12071

902 **Appendix A Notation**

903 Tables A1, A2, A3, A4, and A5 list the notation we use in the poroelasticity for-
 904 mulation.

Table A1: Mathematical notation for poroelasticity with infinitesimal strain, neglecting inertia. Unknown variables.

Symbol	Description	Dimensions
\vec{u}	Displacement field	L
p	Pore fluid pressure field	$\frac{M}{LT^2}$
ϵ_v	Volumetric (trace) strain	–

Table A2: Mathematical notation for poroelasticity with infinitesimal strain, neglecting inertia. Derived quantities.

Symbol	Description	Dimensions
σ	Cauchy stress tensor	$\frac{M}{LT^2}$
ϵ	Cauchy strain tensor	–
ζ	Variation of fluid content (variation of fluid vol. per unit vol. of porous media), $\alpha\epsilon_v + \frac{p}{M}$	–
ρ_b	Bulk density, $(1 - \phi)\rho_s + \phi\rho_f$	$\frac{M}{L^3}$
\vec{q}	Darcy flux, $-\frac{\mathbf{k}}{\mu_f} \cdot (\nabla p - \vec{f}_f)$	$\frac{L}{T}$
M	Biot modulus, $\left(\frac{\phi}{K_f} + \frac{\alpha - \phi}{K_s}\right)^{-1}$	$\frac{M}{LT^2}$
ν	Poisson ratio, drained, $\frac{3K_d - 2\mu}{2(3K_d + \mu)}$	–
ν_u	Poisson ratio, undrained, $\frac{3K_u - 2\mu}{2(3K_u + \mu)}$	–
c	Consolidation coefficient, $\frac{\frac{k}{S}}{\frac{\mu_f}{S}}$	$\frac{L^2}{T}$
S	Storage coefficient, $\frac{1}{M} + \frac{3\alpha^2}{3K_d + 4\mu}$	$\frac{LT^2}{M}$
B	Skempton's Coefficient, $\frac{\alpha M}{(K_d + \alpha^2 M)}$	–

Table A3: Mathematical notation for poroelasticity with infinitesimal strain, neglecting inertia. Common constitutive parameters.

Symbol	Description	Dimensions
ρ_f	Fluid density	$\frac{M}{L^3}$
ρ_s	Solid (matrix) density	$\frac{M}{L^3}$
λ	1st Lamé parameter	$\frac{M}{LT^2}$
μ	Shear modulus	$\frac{M}{LT^2}$
ϕ	Porosity	–
\mathbf{k}	Permeability	L^2
μ_f	Fluid viscosity	$\frac{M}{LT^2} \cdot T$
K_s	Solid grain bulk modulus	$\frac{M}{LT^2}$
K_f	Fluid bulk modulus	$\frac{M}{LT^2}$
K_d	Drained bulk modulus	$\frac{M}{LT^2}$
α	Biot coefficient, $1 - \frac{K_d}{K_s}$	–

Table A4: Mathematical notation for poroelasticity with infinitesimal strain, neglecting inertia. Source terms.

Symbol	Description	Dimensions
\vec{f}	Body force per unit volume, for example: $\rho_b \vec{g}$	$\frac{M}{L^2 T^2}$
\vec{f}_f	Fluid body force, for example: $\rho_f \vec{g}$	$\frac{M}{L^2 T^2}$
γ	Source density; rate of injected fluid per unit volume of the porous solid	$\frac{1}{T}$

Table A5: Mathematical notation for poroelasticity with infinitesimal strain, neglecting inertia. Position terms.

Symbol	Description	Dimensions
x	Position on x axis (Cartesian)	L
y	Position on y axis (Cartesian)	L
z	Position on z axis (Cartesian)	L
t	Position in time	T

905 **Appendix B Method of Manufactured Solutions Test Cases**

 906 **B1 Quadratic Space and Linear Time Solution - S2T1**

 907 **B11 Two Dimensions**

First, we choose solutions for \vec{u} and p ,

$$u_x = x^2, \quad (\text{B1})$$

$$u_y = y^2 - 2xy, \quad (\text{B2})$$

$$p = (x + y)t. \quad (\text{B3})$$

Second, we compute the fields that are derived from the displacement and pore fluid pressure,

$$\epsilon = \begin{bmatrix} \frac{\partial u_x}{\partial x} & \frac{1}{2} \left(\frac{\partial u_x}{\partial y} + \frac{\partial u_y}{\partial x} \right) \\ \frac{1}{2} \left(\frac{\partial u_y}{\partial x} + \frac{\partial u_x}{\partial y} \right) & \frac{\partial u_y}{\partial y} \end{bmatrix} = \begin{bmatrix} 2x & -y \\ -y & 2y - 2x \end{bmatrix}, \quad (\text{B4})$$

$$\epsilon_v = \nabla \cdot \vec{u} = 2y, \quad (\text{B5})$$

$$\vec{q} = -\frac{\mathbf{k}}{\mu_f} \cdot [\nabla p] = -\begin{bmatrix} \frac{k_x}{\mu_f} & 0 \\ 0 & \frac{k_y}{\mu_f} \end{bmatrix} \cdot \begin{bmatrix} t \\ t \end{bmatrix} = -\frac{1}{\mu_f} \begin{bmatrix} k_x \\ k_y \end{bmatrix} t, \quad (\text{B6})$$

$$\zeta = \alpha \epsilon_v + \frac{p}{M} = \alpha (2y) + \frac{(x + y)t}{M}. \quad (\text{B7})$$

We insert our assumed solution definition into the strong form of the quasi-static poroelasticity equations to generate forcing functions. These forcing functions are added to the weak form terms, and we verify that our generated solution matches with the manufactured solution that we initially defined.

$$\nabla \cdot \sigma = \nabla \cdot \left(2\mu \begin{bmatrix} 2x & -y \\ -y & 2y - 2x \end{bmatrix} + \lambda \begin{bmatrix} 2y & 0 \\ 0 & 2y \end{bmatrix} - (x + y) \begin{bmatrix} \alpha t & 0 \\ 0 & \alpha t \end{bmatrix} \right), \quad (\text{B8})$$

$$= 2\mu \begin{bmatrix} 1 \\ 2 \end{bmatrix} + \lambda \begin{bmatrix} 0 \\ 2 \end{bmatrix} - \begin{bmatrix} \alpha t \\ \alpha t \end{bmatrix}, \quad (\text{B9})$$

$$\dot{\zeta} + \nabla \cdot \vec{q} = \frac{\dot{p}}{M} + \alpha \dot{\epsilon}_v + \nabla \cdot \left(-\frac{1}{\mu_f} \begin{bmatrix} k_x \\ k_y \end{bmatrix} t \right) = \frac{(x + y)}{M}, \quad (\text{B10})$$

$$\nabla \cdot \vec{u} - \epsilon_v = 2y - 2y = 0. \quad (\text{B11})$$

B12 Three Dimensions

First, we choose solutions for \vec{u} and p ,

$$u_x = x^2, \quad (\text{B12})$$

$$u_y = y^2 - 2xy, \quad (\text{B13})$$

$$u_z = z^2 - 2yz, \quad (\text{B14})$$

$$p = (x + y + z)t. \quad (\text{B15})$$

Second, we compute the fields that are derived from the displacement and pore fluid pressure,

$$\epsilon = \begin{bmatrix} \frac{\partial u_x}{\partial x} & \frac{1}{2} \left(\frac{\partial u_x}{\partial y} + \frac{\partial u_y}{\partial x} \right) & \frac{1}{2} \left(\frac{\partial u_x}{\partial z} + \frac{\partial u_z}{\partial x} \right) \\ \frac{1}{2} \left(\frac{\partial u_y}{\partial x} + \frac{\partial u_x}{\partial y} \right) & \frac{\partial u_y}{\partial y} & \frac{1}{2} \left(\frac{\partial u_y}{\partial z} + \frac{\partial u_z}{\partial y} \right) \\ \frac{1}{2} \left(\frac{\partial u_z}{\partial x} + \frac{\partial u_x}{\partial z} \right) & \frac{1}{2} \left(\frac{\partial u_z}{\partial y} + \frac{\partial u_y}{\partial z} \right) & \frac{\partial u_z}{\partial z} \end{bmatrix}, \quad (\text{B16})$$

$$= \begin{bmatrix} 2x & -y & 0 \\ -y & 2y - 2x & -z \\ 0 & -z & 2z - 2y \end{bmatrix}, \quad (\text{B17})$$

$$\epsilon_v = \nabla \cdot \vec{u} = 2z, \quad (\text{B18})$$

$$\vec{q} = -\frac{\mathbf{k}}{\mu_f} \cdot [\nabla p] = -\begin{bmatrix} \frac{k_x}{\mu_f} & 0 & 0 \\ 0 & \frac{k_y}{\mu_f} & 0 \\ 0 & 0 & \frac{k_z}{\mu_f} \end{bmatrix} \cdot \begin{bmatrix} t \\ t \\ t \end{bmatrix} = -\frac{1}{\mu_f} \begin{bmatrix} k_x \\ k_y \\ k_z \end{bmatrix} t, \quad (\text{B19})$$

$$\zeta = \alpha \epsilon_v + \frac{p}{M} = \alpha (2z) + \frac{(x + y + z)t}{M}. \quad (\text{B20})$$

We insert our assumed solution definition into the strong form of the quasi-static poroelasticity equations to generate forcing functions. These forcing functions are added to the weak form terms, and we verify that our generated solution matches with the man-

ufactured solution that we initially defined.

$$\nabla \cdot \sigma = \nabla \cdot \left(2\mu \begin{bmatrix} 2x & -y & 0 \\ -y & 2y - 2x & -z \\ 0 & -z & 2z - 2y \end{bmatrix} + \lambda \begin{bmatrix} 2z & 0 & 0 \\ 0 & 2z & 0 \\ 0 & 0 & 2z \end{bmatrix} - (x + y + z) \begin{bmatrix} \alpha t & 0 & 0 \\ 0 & \alpha t & 0 \\ 0 & 0 & \alpha t \end{bmatrix} \right), \quad (\text{B21})$$

$$= 2\mu \begin{bmatrix} 1 \\ 1 \\ 2 \end{bmatrix} + \lambda \begin{bmatrix} 0 \\ 0 \\ 2 \end{bmatrix} - \begin{bmatrix} \alpha t \\ \alpha t \\ \alpha t \end{bmatrix} \quad (\text{B22})$$

$$\dot{\zeta} + \nabla \cdot \vec{q} = \frac{\dot{p}}{M} + \alpha \dot{\epsilon}_v + \nabla \cdot \left(-\frac{1}{\mu_f} \begin{bmatrix} k_x \\ k_y \\ k_z \end{bmatrix} t \right) = \frac{(x + y + z)}{M}, \quad (\text{B23})$$

$$\nabla \cdot \vec{u} - \epsilon_v = 2z - 2z = 0. \quad (\text{B24})$$

909

B2 Quadratic Space and Trigonometric Time Solution - S2Tt

910

B21 Two Dimensions

First, we choose the following solutions for the variables \vec{u} and p ,

$$u_x = x^2, \quad (\text{B25})$$

$$u_y = y^2 - 2xy, \quad (\text{B26})$$

$$p = (x + y) \cos(t). \quad (\text{B27})$$

Second, we compute the fields that are derived from the displacement and pore fluid pressure,

$$\epsilon = \begin{bmatrix} \frac{\partial u_x}{\partial x} & \frac{1}{2} \left(\frac{\partial u_x}{\partial y} + \frac{\partial u_y}{\partial x} \right) \\ \frac{1}{2} \left(\frac{\partial u_y}{\partial x} + \frac{\partial u_x}{\partial y} \right) & \frac{\partial u_y}{\partial y} \end{bmatrix} = \begin{bmatrix} 2x & -y \\ -y & 2y - 2x \end{bmatrix}, \quad (\text{B28})$$

$$\epsilon_v = \nabla \cdot \vec{u} = 2y \quad (\text{B29})$$

$$\vec{q} = -\frac{\mathbf{k}}{\mu_f} \cdot [\nabla p] = -\begin{bmatrix} \frac{k_x}{\mu_f} & 0 \\ 0 & \frac{k_y}{\mu_f} \end{bmatrix} \cdot \begin{bmatrix} \cos(t) \\ \cos(t) \end{bmatrix} = -\frac{1}{\mu_f} \begin{bmatrix} k_x \\ k_y \end{bmatrix} \cos(t), \quad (\text{B30})$$

$$\zeta = \alpha \epsilon_v + \frac{p}{M} = \alpha (2y) + \frac{(x + y) \cos(t)}{M}. \quad (\text{B31})$$

We insert our assumed solution definition into the strong form of the quasi-static poroelasticity equations to generate forcing functions. These forcing functions are added to the weak form terms and we then check that our generated solution matches with the

manufactured solution that we initially defined.

$$\nabla \cdot \sigma = \nabla \cdot \left(2\mu \begin{bmatrix} 2x & -y \\ -y & 2y - 2x \end{bmatrix} + \lambda \begin{bmatrix} 2y & 0 \\ 0 & 2y \end{bmatrix} - (x + y) \begin{bmatrix} \alpha \cos(t) & 0 \\ 0 & \alpha \cos(t) \end{bmatrix} \right), \quad (\text{B32})$$

$$= 2\mu \begin{bmatrix} 1 \\ 2 \end{bmatrix} + \lambda \begin{bmatrix} 0 \\ 2 \end{bmatrix} - \begin{bmatrix} \alpha \cos(t) \\ \alpha \cos(t) \end{bmatrix} \quad (\text{B33})$$

$$\dot{\zeta} + \nabla \cdot \vec{q} = \frac{\dot{p}}{M} + \alpha \dot{\epsilon}_v + \nabla \cdot \left(-\frac{1}{\mu_f} \begin{bmatrix} k_x \\ k_y \end{bmatrix} \cos(t) \right) = \frac{-\sin(t)(x + y)}{M}, \quad (\text{B34})$$

$$\nabla \cdot \vec{u} - \epsilon_v = 2y - 2y = 0. \quad (\text{B35})$$

911

B22 Three Dimensions

First, we choose the following solutions for the variables \vec{u} and p ,

$$u_x = x^2, \quad (\text{B36})$$

$$u_y = y^2 - 2xy, \quad (\text{B37})$$

$$u_z = z^2 - 2yz, \quad (\text{B38})$$

$$p = (x + y + z) \cos(t). \quad (\text{B39})$$

Second, we compute the fields that are derived from the displacement and pore fluid pressure,

$$\epsilon = \begin{bmatrix} \frac{\partial u_x}{\partial x} & \frac{1}{2} \left(\frac{\partial u_x}{\partial y} + \frac{\partial u_y}{\partial x} \right) & \frac{1}{2} \left(\frac{\partial u_x}{\partial z} + \frac{\partial u_z}{\partial x} \right) \\ \frac{1}{2} \left(\frac{\partial u_y}{\partial x} + \frac{\partial u_x}{\partial y} \right) & \frac{\partial u_y}{\partial y} & \frac{1}{2} \left(\frac{\partial u_y}{\partial z} + \frac{\partial u_z}{\partial y} \right) \\ \frac{1}{2} \left(\frac{\partial u_z}{\partial x} + \frac{\partial u_x}{\partial z} \right) & \frac{1}{2} \left(\frac{\partial u_z}{\partial y} + \frac{\partial u_y}{\partial z} \right) & \frac{\partial u_z}{\partial z} \end{bmatrix} = \begin{bmatrix} 2x & -y & 0 \\ -y & 2y - 2x & -z \\ 0 & -z & 2z - 2y \end{bmatrix}, \quad (\text{B40})$$

$$\epsilon_v = \nabla \cdot \vec{u} = 2z, \quad (\text{B41})$$

$$\vec{q} = -\frac{\mathbf{k}}{\mu_f} \cdot [\nabla p] = -\begin{bmatrix} \frac{k_x}{\mu_f} & 0 & 0 \\ 0 & \frac{k_y}{\mu_f} & 0 \\ 0 & 0 & \frac{k_z}{\mu_f} \end{bmatrix} \cdot \begin{bmatrix} \cos(t) \\ \cos(t) \\ \cos(t) \end{bmatrix} = -\frac{1}{\mu_f} \begin{bmatrix} k_x \\ k_y \\ k_z \end{bmatrix} \cos(t), \quad (\text{B42})$$

$$\zeta = \alpha \epsilon_v + \frac{p}{M} = \alpha(2z) + \frac{(x + y + z) \cos(t)}{M}. \quad (\text{B43})$$

We insert our assumed solution definition into the strong form of the quasi-static poroelasticity equations to generate forcing functions. These forcing functions are added to the weak form terms and we then check that our generated solution matches with the

manufactured solution that we initially defined.

$$\nabla \cdot \sigma = \nabla \cdot \left(2\mu \begin{bmatrix} 2x & -y & 0 \\ -y & 2y - 2x & -z \\ 0 & -z & 2z - 2y \end{bmatrix} + \lambda \begin{bmatrix} 2z & 0 & 0 \\ 0 & 2z & 0 \\ 0 & 0 & 2z \end{bmatrix} \right) \quad (\text{B44})$$

$$- (x + y + z) \begin{bmatrix} \alpha \cos(t) & 0 & 0 \\ 0 & \alpha \cos(t) & 0 \\ 0 & 0 & \alpha \cos(t) \end{bmatrix},$$

$$= 2\mu \begin{bmatrix} 1 \\ 1 \\ 2 \end{bmatrix} + \lambda \begin{bmatrix} 0 \\ 0 \\ 2 \end{bmatrix} - \begin{bmatrix} \alpha \cos(t) \\ \alpha \cos(t) \\ \alpha \cos(t) \end{bmatrix}, \quad (\text{B45})$$

$$\dot{\zeta} + \nabla \cdot \vec{q} = \frac{\dot{p}}{M} + \alpha \dot{\epsilon}_v + \nabla \cdot \left(-\frac{1}{\mu_f} \begin{bmatrix} k_x \\ k_y \\ k_z \end{bmatrix} \cos(t) \right) = \frac{(x + y + z)}{M}, \quad (\text{B46})$$

$$\nabla \cdot \vec{u} - \epsilon_v = 2z - 2z = 0. \quad (\text{B47})$$

912

B3 Trigonometric Space and Linear Time Solution - StT1

913

B31 Two Dimensions

First, we choose the following solutions for the variables \vec{u} and p ,

$$u_x = \sin(2\pi x) \quad (\text{B48})$$

$$u_y = \sin(2\pi y) - 2xy \quad (\text{B49})$$

$$p = (\cos(2\pi x) + \cos(2\pi y)) t \quad (\text{B50})$$

Second, we compute the fields that are derived from the displacement and pore fluid pressure,

$$\epsilon = \begin{bmatrix} \frac{\partial u_x}{\partial x} & \frac{1}{2} \left(\frac{\partial u_x}{\partial y} + \frac{\partial u_y}{\partial x} \right) \\ \frac{1}{2} \left(\frac{\partial u_y}{\partial x} + \frac{\partial u_x}{\partial y} \right) & \frac{\partial u_y}{\partial y} \end{bmatrix} = \begin{bmatrix} 2\pi \cos(2\pi x) & -y \\ -y & 2\pi \cos(2\pi y) - 2x \end{bmatrix} \quad (\text{B51})$$

$$\epsilon_v = \nabla \cdot \vec{u} = 2\pi [\cos(2\pi x) + \cos(2\pi y)] - 2x \quad (\text{B52})$$

$$\vec{q} = -\frac{\mathbf{k}}{\mu_f} \cdot [\nabla p] = -\begin{bmatrix} \frac{k_x}{\mu_f} & 0 \\ 0 & \frac{k_y}{\mu_f} \end{bmatrix} \cdot \begin{bmatrix} -2\pi t \sin(2\pi x) \\ -2\pi t \sin(2\pi y) \end{bmatrix} = \frac{2\pi t}{\mu_f} \begin{bmatrix} k_x \sin(2\pi x) \\ k_y \sin(2\pi y) \end{bmatrix} \quad (\text{B53})$$

$$\zeta = \alpha \epsilon_v + \frac{p}{M} = \alpha (2\pi [\cos(2\pi x) + \cos(2\pi y)] - 2x) + \frac{[\cos(2\pi x) + \cos(2\pi y)] t}{M} \quad (\text{B54})$$

We insert our assumed solution definition into the strong form of the quasi-static poroelasticity equations to generate forcing functions. These forcing functions are added to the weak form terms and we then check that our generated solution matches with the

manufactured solution that we initially defined.

$$\nabla \cdot \sigma = \nabla \cdot \left(2\mu \begin{bmatrix} 2\pi \cos(2\pi x) & -y \\ -y & 2\pi \cos(2\pi y) - 2x \end{bmatrix} + \lambda \begin{bmatrix} \epsilon_v & 0 \\ 0 & \epsilon_v \end{bmatrix} - \alpha \begin{bmatrix} p & 0 \\ 0 & p \end{bmatrix} \right) \quad (\text{B55})$$

$$= 2\mu \begin{bmatrix} -4\pi^2 \sin(2\pi x) - 1 \\ -4\pi^2 \sin(2\pi y) \end{bmatrix} + \lambda \begin{bmatrix} -4\pi^2 \sin(2\pi x) - 2 \\ -4\pi^2 \sin(2\pi x) \end{bmatrix} - \alpha \begin{bmatrix} 2\pi t \sin(2\pi x) \\ 2\pi t \sin(2\pi y) \end{bmatrix} \quad (\text{B56})$$

$$\dot{\zeta} + \nabla \cdot \vec{q} = \frac{\dot{p}}{M} + \alpha \dot{\epsilon}_v + \nabla \cdot \left(-\frac{\mathbf{k}}{\mu_f} \cdot \nabla p \right) \quad (\text{B57})$$

$$= \frac{[\cos(2\pi x) + \cos(2\pi y)]}{M} + \nabla \cdot \left(\begin{bmatrix} -\frac{k_x}{\mu_f} & 0 \\ 0 & -\frac{k_y}{\mu_f} \end{bmatrix} \cdot \begin{bmatrix} -2\pi t \sin(2\pi x) \\ -2\pi t \sin(2\pi y) \end{bmatrix} \right) \quad (\text{B58})$$

$$= \frac{[\cos(2\pi x) + \cos(2\pi y)]}{M} + \frac{4\pi^2 k_x t}{\mu_f} \cos(2\pi x) + \frac{4\pi^2 k_y t}{\mu_f} \cos(2\pi y) \quad (\text{B59})$$

$$\nabla \cdot \vec{u} - \epsilon_v = 2\pi [\cos(2\pi x) + \cos(2\pi y)] - 2x - 2\pi [\cos(2\pi x) + \cos(2\pi y)] - 2x = 0. \quad (\text{B60})$$

914

B32 Three Dimensions

First, we choose the following solutions for the variables \vec{u} and p ,

$$u_x = \sin(2\pi x) \quad (\text{B61})$$

$$u_y = \sin(2\pi y) - 2xy \quad (\text{B62})$$

$$u_z = \sin(2\pi z) - 2yz \quad (\text{B63})$$

$$p = [\cos(2\pi x) + \cos(2\pi y) + \cos(2\pi z)] t \quad (\text{B64})$$

Second, we compute the fields that are derived from the displacement and pore fluid pressure,

$$\epsilon = \begin{bmatrix} \frac{\partial u_x}{\partial x} & \frac{1}{2} \left(\frac{\partial u_x}{\partial y} + \frac{\partial u_y}{\partial x} \right) & \frac{1}{2} \left(\frac{\partial u_x}{\partial z} + \frac{\partial u_z}{\partial x} \right) \\ \frac{1}{2} \left(\frac{\partial u_y}{\partial x} + \frac{\partial u_x}{\partial y} \right) & \frac{\partial u_y}{\partial y} & \frac{1}{2} \left(\frac{\partial u_y}{\partial z} + \frac{\partial u_z}{\partial y} \right) \\ \frac{1}{2} \left(\frac{\partial u_z}{\partial x} + \frac{\partial u_x}{\partial z} \right) & \frac{1}{2} \left(\frac{\partial u_z}{\partial y} + \frac{\partial u_y}{\partial z} \right) & \frac{\partial u_z}{\partial z} \end{bmatrix} \quad (\text{B65})$$

$$= \begin{bmatrix} 2\pi \cos(2\pi x) & -y & 0 \\ -y & 2\pi \cos(2\pi y) - 2x & -y \\ 0 & -y & 2\pi \cos(2\pi z) - 2y \end{bmatrix} \quad (\text{B66})$$

$$\epsilon_v = \nabla \cdot \vec{u} = 2\pi [\cos(2\pi x) + \cos(2\pi y) + \cos(2\pi z)] - 2x - 2y \quad (\text{B67})$$

$$\vec{q} = -\frac{\mathbf{k}}{\mu_f} \cdot [\nabla p] = - \begin{bmatrix} \frac{k_x}{\mu_f} & 0 & 0 \\ 0 & \frac{k_y}{\mu_f} & 0 \\ 0 & 0 & \frac{k_z}{\mu_f} \end{bmatrix} \cdot \begin{bmatrix} -2\pi t \sin(2\pi x) \\ -2\pi t \sin(2\pi y) \\ -2\pi t \sin(2\pi z) \end{bmatrix} = \frac{2\pi t}{\mu_f} \begin{bmatrix} k_x \sin(2\pi x) \\ k_y \sin(2\pi y) \\ k_z \sin(2\pi z) \end{bmatrix} \quad (\text{B68})$$

$$\zeta = \alpha \epsilon_v + \frac{p}{M} = \alpha (2\pi [\cos(2\pi x) + \cos(2\pi y) + \cos(2\pi z)] - 2x - 2y) + \frac{[\cos(2\pi x) + \cos(2\pi y) + \cos(2\pi z)] t}{M} \quad (\text{B69})$$

We insert our assumed solution definition into the strong form of the quasi-static poroelasticity equations to generate forcing functions. These forcing functions are added to the weak form terms and we then check that our generated solution matches with the

manufactured solution that we initially defined.

$$\nabla \cdot \sigma = \nabla \cdot \left(2\mu \begin{bmatrix} 2\pi \cos(2\pi x) & -y & 0 \\ -y & 2\pi \cos(2\pi y) - 2x & -y \\ 0 & -y & 2\pi \cos(2\pi z) - 2y \end{bmatrix} \right) \quad (\text{B70})$$

$$+ \lambda \begin{bmatrix} \epsilon_v & 0 & 0 \\ 0 & \epsilon_v & 0 \\ 0 & 0 & \epsilon_v \end{bmatrix} - \alpha \begin{bmatrix} p & 0 & 0 \\ 0 & p & 0 \\ 0 & 0 & p \end{bmatrix} \Bigg),$$

$$= 2\mu \begin{bmatrix} -4\pi^2 \sin(2\pi x) - 1 \\ -4\pi^2 \sin(2\pi y) \\ -1 - 4\pi^2 \sin(2\pi y) \end{bmatrix} + \lambda \begin{bmatrix} -4\pi^2 \sin(2\pi x) - 2 \\ -4\pi^2 \sin(2\pi y) - 2 \\ -4\pi^2 \sin(2\pi z) \end{bmatrix} - \alpha \begin{bmatrix} 2\pi t \sin(2\pi x) \\ 2\pi t \sin(2\pi y) \\ 2\pi t \sin(2\pi z) \end{bmatrix}, \quad (\text{B71})$$

$$\dot{\zeta} + \nabla \cdot \vec{q} = \frac{\dot{p}}{M} + \alpha \dot{\epsilon}_v + \nabla \cdot \left(-\frac{\mathbf{k}}{\mu_f} \cdot \nabla p \right) \quad (\text{B72})$$

$$= \frac{[\cos(2\pi x) + \cos(2\pi y) + \cos(2\pi z)]}{M} \quad (\text{B73})$$

$$+ \nabla \cdot \left(\begin{bmatrix} -\frac{k_x}{\mu_f} & 0 & 0 \\ 0 & -\frac{k_y}{\mu_f} & 0 \\ 0 & 0 & -\frac{k_z}{\mu_f} \end{bmatrix} \cdot \begin{bmatrix} -2\pi t \sin(2\pi x) \\ -2\pi t \sin(2\pi y) \\ -2\pi t \sin(2\pi z) \end{bmatrix} \right)$$

$$= \frac{[\cos(2\pi x) + \cos(2\pi y) + \cos(2\pi z)]}{M} \quad (\text{B74})$$

$$+ \frac{4\pi t}{\mu_f} [k_x \cos(2\pi x) + k_y \cos(2\pi y) + k_z \cos(2\pi z)],$$

$$\nabla \cdot \vec{u} - \epsilon_v = 2\pi [\cos(2\pi x) + \cos(2\pi y) + \cos(2\pi z)] - 2x - 2y \quad (\text{B75})$$

$$- 2\pi [\cos(2\pi x) + \cos(2\pi y) + \cos(2\pi z)] - 2x - 2y = 0.$$

915 Appendix C Terzaghi's Problem

We write Terzaghi's problem (von Terzaghi, 1923) as

$$\sigma_{zz} = -P_0 H(t) \text{ and } p = 0 \text{ for } z = 0 \text{ and } t \geq 0, \quad (\text{C1})$$

$$u_z = 0 \text{ and } \frac{\partial p}{\partial z} = 0 \text{ for } z = L \text{ and } t \geq 0, \quad (\text{C2})$$

$$p = 0 \text{ for } 0 \leq z \leq L \text{ and } t = 0^-, \quad (\text{C3})$$

916 where P_0 refers to the magnitude of the normal traction, and $H(t)$ refers to the Heav-
917 iside step function (Abramowitz & Stegun, 1964).

918 C1 Pore Pressure Solution

The applied normal traction is $\sigma_{zz} = -P_0$ for $t > 0$, and we arrive at the following homogeneous diffusion equation for pore pressure:

$$\dot{p} - c \frac{\partial^2 p}{\partial z^2} = 0. \quad (\text{C4})$$

Using the intuition provided from the Skempton effect (Skempton, 1954), a pore pressure increase should occur at the instant when loading is applied, giving the initial condition

$$p(z, 0^+) = \frac{P_0 \eta}{\mu S}. \quad (\text{C5})$$

The solution to the pore pressure diffusion equation is

$$p(z, t) = \frac{P_0 \eta}{\mu S} F_1(z^* t^*), \quad (\text{C6})$$

with the summation term

$$F_1(z^*, t^*) = \sum_{m=1,3,\dots}^{\infty} \frac{4}{m\pi} \sin\left(\frac{m\pi z^*}{2}\right) e^{-m^2 \pi^2 t^*}, \quad (\text{C7})$$

919 and dimensionless time and distance terms defined as $t^* = \frac{ct}{4L^2}$ and $z^* = \frac{z}{L}$, respec-
920 tively.

921 C2 Displacement

From the boundary conditions, we recognize that $u_x = 0$. We compute u_y by substituting in the solution for the pore fluid pressure into the differential equation for the displacement (Cheng et al., 2017),

$$\frac{2\mu(1-\nu)}{1-2\nu} \frac{\partial^2 u_z}{\partial z^2} - \alpha \frac{\partial p}{\partial z} = 0. \quad (\text{C8})$$

Substituting the solution for pressure into the above equation and integrating twice with respect to z , while making use of the boundary conditions leads to

$$u_z(z, t) = \frac{P_0 L (1-2\nu)}{2\mu(1-\nu_u)} (1-z^*) + \frac{P_0 L (\nu_u - \nu)}{2\mu(1-\nu_u)(1-\nu)} F_2(z^*, t^*), \quad (\text{C9})$$

with the infinite series term defined as

$$F_2(z^*, t^*) = \sum_{m=1,3,\dots}^{\infty} \frac{8}{m^2 \pi^2} \cos\left(\frac{m\pi z^*}{2}\right) e^{-m^2 \pi^2 t^*}. \quad (\text{C10})$$

922 Appendix D Mandel's Problem

We express the boundary conditions as

$$\sigma_{xx} = \sigma_{xy} = 0 \text{ at } x = \pm a, \quad (\text{D1})$$

$$\sigma_{xy} = q_y = 0 \text{ at } y = \pm b, \quad (\text{D2})$$

$$u_y = u_y(t) \text{ at } y = \pm b, \quad (\text{D3})$$

$$\int_{-a}^a \sigma_{yy} dx = -2F \text{ at } y = \pm b. \quad (\text{D4})$$

923 Especially noteworthy are the boundary conditions defined at $y = \pm b$. The rigid plate
924 boundary condition means that we know that the y displacement is independent of x .

925 The subsequent condition states that while the magnitude of the force applied in the ver-
 926 tical direction is known, the local distribution of the vertical stress imposed at the bound-
 927 ary is not known. We work around this by prescribing the displacement on the vertical
 928 boundary to that predicted by the analytical solution.

Knowing that the y displacement is independent of x , we have

$$u_x = f(\vec{x}, t), \quad u_y = C(t)y; \quad (D5)$$

$$\epsilon_{yy} = \epsilon_{yy}(t), \quad q_y = 0; \quad (D6)$$

$$\epsilon_{xx} = \epsilon_{xx}(\vec{x}, t), \quad q_x = q_x(\vec{x}, t); \quad (D7)$$

$$\sigma_{yy} = \sigma_{yy}(\vec{x}, t), \quad p = p(\vec{x}, t), \quad \sigma_{xx} = \sigma_{xy} = 0, \quad (D8)$$

929 where $C(t)$ refers to the prescribed displacement as given by the analytical solu-
 930 tion.

Mandel (1953) considered incompressible constituents and derived the solution for the pore pressure only. We consider both a compressible fluid and compressible solid and derive the solution for both the pore pressure and displacement. At the instant $t = 0+$ we apply the compressive normal traction and the resultant pore pressure jump leads to the initial conditions

$$p_0(\vec{x}, 0) = \frac{1}{3a}B(1 + \nu_u)F, \quad (D9)$$

$$u_{x,0}(\vec{x}, 0) = \frac{F\nu_u}{2\mu} \frac{x}{a}, \quad (D10)$$

$$u_{y,0}(\vec{x}, 0) = -\frac{F(1 - \nu_u)}{2\mu} \frac{y}{a}. \quad (D11)$$

Here Skempton's coefficient is defined as $B = \frac{\alpha M}{(K_d + \alpha^2 M)}$, and the undrained Poisson ratio as $\nu_u = \frac{3\nu + \alpha B(1 - 2\nu)}{3 - \alpha B(1 - 2\nu)}$. This results in analytical solutions for pressure and displacement of the form

$$p(x, y, t) = 2p_0 \sum_{n=1}^{\infty} \frac{\sin \theta_n}{\theta_n - \sin \theta_n \cos \theta_n} \left[\cos \left(\frac{\theta_n x}{a} \right) - \cos \theta_n \right] e^{-\frac{\theta_n^2 c_f t}{a^2}}, \quad (D12)$$

$$u_x(x, y, t) = \left(\frac{F\nu}{2\mu a} - \frac{F\nu_u}{\mu a} \sum_{n=1}^{\infty} \frac{\sin \theta_n \cos \theta_n}{\theta_n - \sin \theta_n \cos \theta_n} e^{-\frac{\theta_n^2 c_f t}{a^2}} \right) x \quad (D13)$$

$$+ \frac{F}{\mu} \sum_{n=1}^{\infty} \frac{\cos \theta_n}{\theta_n - \sin \theta_n \cos \theta_n} \sin \frac{\theta_n x}{a} e^{-\frac{\theta_n^2 c_f t}{a^2}},$$

$$u_y(x, y, t) = \left(-\frac{F(1 - \nu)}{2\mu a} + \frac{F(1 - \nu_u)}{\mu a} \sum_{n=1}^{\infty} \frac{\sin \theta_n \cos \theta_n}{\theta_n - \sin \theta_n \cos \theta_n} e^{-\frac{\theta_n^2 c_f t}{a^2}} \right) y. \quad (D14)$$

Appendix E Cryer's Problem

We apply a radial traction at $t = 0$ to an undisturbed domain,

$$\sigma_{rr} = -P_0 H(t) \text{ and } p = 0 \text{ at } r = r_0, \quad (\text{E1})$$

$$u_r = 0 \text{ and } \frac{\partial p}{\partial r} = 0 \text{ at } r = 0, \quad (\text{E2})$$

where the subscript "r" refers to radial, and r_0 is the radius of the sphere under consideration. The superscript "*" denotes that a value is dimensionless, resulting in dimensionless radial length $r^* = \frac{r}{r_0}$, and dimensionless time $t^* = \frac{ct^2}{r_0^2}$. Once again, the subscripts "d" and "u" represent drained and undrained respectively. Cheng (2016) derives the analytical solution, so we only summarize the solutions for displacement and pressure for the case involving compressible constituents. Following that reference, we define the drained Poisson ratio, $\eta = \frac{3K_d - 2\mu}{2(3K_d + 4\mu)}$, the undrained Poisson ratio $\eta_u = \frac{3K_u - 2\mu}{2(3K_u + 4\mu)}$, the consolidation coefficient $c = \frac{\left(\frac{k}{\mu_f}\right)}{S}$, and the storage coefficient $S = \frac{1}{M} + \frac{3\alpha^2}{3K_d + \mu}$. The permeability k is an isotropic value. Solutions vary only as a function of time and distance from the center of the sphere and thus we only model one-eighth of the sphere.

$$\frac{p(r, t)}{P_0} = \sum_{n=1}^{\infty} \frac{18(\nu_u - \nu)^2}{\eta E(x_n)} \left[\frac{\sin(r^* \sqrt{x_n})}{r^* \sin \sqrt{x_n}} \right] e^{-x_n t^*} \quad (\text{E3})$$

$$\begin{aligned} \frac{u_r(r, t)}{u_r(r_0, \infty)} &= r^* - \sum_{n=1}^{\infty} \frac{12(1 + \nu)(\nu_u - \nu)}{(1 - 2\nu) E(x_n) r^{*2} x_n \sin \sqrt{x_n}} \\ &\times [3(\nu_u - \nu) [\sin(r^* \sqrt{x_n}) - r^* \sqrt{x_n} \cos(r^* \sqrt{x_n})] \\ &+ (1 - \nu)(1 - 2\nu) r^{*3} x_n \sin \sqrt{x_n}] e^{-x_n t^*} \end{aligned} \quad (\text{E4})$$

with

$$E(x_n) = (1 - \nu)^2 (1 + \nu_u)^2 x_n - 18(1 + \nu)(\nu_u - \nu)(1 - \nu_u) \quad (\text{E5})$$

where x_n refers to the positive roots of the algebraic equation

$$\tan \sqrt{x_n} = \frac{6(\nu_u - \nu) \sqrt{x_n}}{6(\nu_u - \nu) - (1 - \nu)(1 + \nu_u) x_n} \quad (\text{E6})$$

for $x_n > 0$.

Appendix F Jacobian Equations

For implicit time stepping with PETSc (Balay et al., 2023b), we write the left hand side Jacobian as

$$\begin{aligned} J_F &= \int_{\Omega} \vec{\psi} \cdot \mathbf{J}_{f_0}(t, s, \dot{s}) \cdot \vec{\psi} + \vec{\psi} \cdot \mathbf{J}_{f_1}(t, s, \dot{s}) : \nabla \vec{\psi} + \nabla \vec{\psi} : \mathbf{J}_{f_2}(t, s, \dot{s}) \cdot \vec{\psi} \\ &+ \nabla \vec{\psi} : \mathbf{J}_{f_3}(t, s, \dot{s}) : \nabla \vec{\psi} \, d\Omega. \end{aligned} \quad (\text{F1})$$

For our poroelasticity implementation with three solution fields, we have 7 nonzero Jacobians:

$$J_F^{uu} = \frac{\partial F^u}{\partial u} + t_{shift} \frac{\partial F^u}{\partial \dot{u}} \quad (\text{F2})$$

$$= \int_{\Omega} \nabla \vec{\psi}^u : \frac{\partial}{\partial u} [-\boldsymbol{\sigma}(\vec{u}, p, \epsilon_v)] d\Omega \quad (\text{F3})$$

$$= \int_{\Omega} \nabla \vec{\psi}^u : \frac{\partial}{\partial u} [-(\mathbf{C} : \boldsymbol{\varepsilon} - \alpha p \mathbf{I})] d\Omega \quad (\text{F4})$$

$$= \int_{\Omega} \nabla \vec{\psi}^u : -\mathbf{C} : \frac{1}{2} (\nabla + \nabla^T) \vec{\psi}^u d\Omega \quad (\text{F5})$$

$$= \int_{\Omega} \psi^u_{i,k} \underbrace{-C_{ikjl}}_{J_{f3}^{uu}} \psi^u_{j,l} d\Omega \quad (\text{F6})$$

$$J_F^{up} = \frac{\partial F^u}{\partial p} + t_{shift} \frac{\partial F^u}{\partial \dot{p}} \quad (\text{F7})$$

$$= \int_{\Omega} \nabla \vec{\psi}^u : \frac{\partial}{\partial p} [-\boldsymbol{\sigma}(\vec{u}, p, \epsilon_v)] d\Omega \quad (\text{F8})$$

$$= \int_{\Omega} \nabla \vec{\psi}^u : \frac{\partial}{\partial p} [-(\mathbf{C} : \boldsymbol{\varepsilon} - \alpha p \mathbf{I})] d\Omega \quad (\text{F9})$$

$$= \int_{\Omega} \nabla \vec{\psi}^u : \alpha \mathbf{I} \psi^p d\Omega \quad (\text{F10})$$

$$= \int_{\Omega} \psi^u_{i,k} \underbrace{(\alpha \delta_{ij})}_{J_{f2}^{up}} \psi^p d\Omega \quad (\text{F11})$$

$$J_F^{u\epsilon_v} = \frac{\partial F^u}{\partial \epsilon_v} + t_{shift} \frac{\partial F^u}{\partial \dot{\epsilon}_v} \quad (\text{F12})$$

$$= \int_{\Omega} \nabla \vec{\psi}^u : \frac{\partial}{\partial \epsilon_v} [-\boldsymbol{\sigma}(\vec{u}, p, \epsilon_v)] d\Omega \quad (\text{F13})$$

$$= \int_{\Omega} \nabla \vec{\psi}^u : \frac{\partial}{\partial \epsilon_v} [-(\mathbf{C} : \boldsymbol{\varepsilon} - \alpha p \mathbf{I})] d\Omega \quad (\text{F14})$$

$$= \int_{\Omega} \nabla \vec{\psi}^u : \frac{\partial}{\partial \epsilon_v} [-(2\mu\boldsymbol{\varepsilon} + \lambda \mathbf{I} \epsilon_v - \alpha p \mathbf{I})] d\Omega \quad (\text{F15})$$

$$= \int_{\Omega} \nabla \vec{\psi}^u : -\lambda \mathbf{I} \psi^{\epsilon_v} d\Omega \quad (\text{F16})$$

$$= \int_{\Omega} \psi^u_{i,j} \underbrace{(-\lambda \delta_{ij})}_{J_{f2}^{u\epsilon_v}} \psi^{\epsilon_v} d\Omega \quad (\text{F17})$$

$$J_F^{pp} = \frac{\partial F^p}{\partial p} + t_{shift} \frac{\partial F^p}{\partial \dot{p}} \quad (\text{F18})$$

$$= \int_{\Omega} \frac{\partial}{\partial p} \left[\psi^p \left(\frac{\partial \zeta(\vec{u}, p_f)}{\partial t} - \gamma(\vec{x}, t) \right) + \nabla \psi^p \cdot -\vec{q}(p) \right] d\Omega \quad (\text{F19})$$

$$+ t_{shift} \int_{\Omega} \frac{\partial}{\partial \dot{p}} \left[\psi^p \left(\dot{\zeta}(\vec{u}, p_f) - \gamma(\vec{x}, t) \right) + \nabla \psi^p \cdot -\vec{q}(p) \right] d\Omega \quad (\text{F20})$$

$$= \int_{\Omega} \frac{\partial}{\partial p} [\nabla \psi^p \cdot -\vec{q}(p)] d\Omega + t_{shift} \int_{\Omega} \frac{\partial}{\partial \dot{p}} \left[\psi^p \left(\dot{\zeta}(\vec{u}, p_f) - \gamma(\vec{x}, t) \right) \right] d\Omega \quad (\text{F21})$$

$$= \int_{\Omega} \frac{\partial}{\partial p} \left[\nabla \psi^p \cdot \left[- \left(-\frac{\mathbf{k}}{\mu_f} \cdot \nabla p \right) \right] \right] d\Omega + t_{shift} \int_{\Omega} \frac{\partial}{\partial \dot{p}} \left[\psi^p \left(\alpha \dot{\epsilon}_v + \frac{\dot{p}}{M} \right) \right] d\Omega \quad (\text{F22})$$

$$= \int_{\Omega} \nabla \psi^p \cdot \underbrace{\frac{\mathbf{k}}{\mu_f}}_{J_{f3}^{pp}} \cdot \nabla \psi^p d\Omega + \int_{\Omega} \underbrace{\psi^p t_{shift} \frac{1}{M}}_{J_{f0}^{pp}} \psi^p d\Omega \quad (\text{F23})$$

$$J_F^{p\epsilon_v} = \frac{\partial F^p}{\partial \epsilon_v} + t_{shift} \frac{\partial F^p}{\partial \dot{\epsilon}_v} \quad (\text{F24})$$

$$= t_{shift} \int_{\Omega} \frac{\partial}{\partial \dot{\epsilon}_v} \left[\psi^p \left(\dot{\zeta}(\vec{u}, p_f) - \gamma(\vec{x}, t) \right) + \nabla \psi^p \cdot -\vec{q}(p) \right] d\Omega \quad (\text{F25})$$

$$= t_{shift} \int_{\Omega} \frac{\partial}{\partial \dot{\epsilon}_v} \left[\psi^p \left(\alpha \dot{\epsilon}_v + \frac{\dot{p}}{M} \right) \right] d\Omega \quad (\text{F26})$$

$$= \int_{\Omega} \underbrace{\psi^p t_{shift} \alpha}_{J_{f0}^{p\epsilon_v}} \psi^{\epsilon_v} d\Omega \quad (\text{F27})$$

$$J_F^{\epsilon_v u} = \frac{\partial F^{\epsilon_v}}{\partial u} + t_{shift} \frac{\partial F^{\epsilon_v}}{\partial \dot{u}} \quad (\text{F28})$$

$$= \int_{\Omega} \psi^{\epsilon_v} \cdot \frac{\partial}{\partial u} (\nabla \cdot \vec{u} - \epsilon_v) d\Omega \quad (\text{F29})$$

$$= \int_{\Omega} \psi_{trial}^{\epsilon_v} (\nabla \cdot \vec{\psi}_{basis}^u) d\Omega \quad (\text{F30})$$

$$= \int_{\Omega} \psi^{\epsilon_v} \underbrace{(\delta_{jl})}_{J_{f1}^{\epsilon_v u}} \psi_{j,l}^u d\Omega, \quad (\text{F31})$$

$$J_F^{\epsilon_v \epsilon_v} = \frac{\partial F^{\epsilon_v}}{\partial \epsilon_v} + t_{shift} \frac{\partial F^{\epsilon_v}}{\partial \dot{\epsilon}_v} \quad (\text{F32})$$

$$= \int_{\Omega} \psi^{\epsilon_v} \cdot \frac{\partial}{\partial \epsilon_v} (\nabla \cdot \vec{u} - \epsilon_v) d\Omega \quad (\text{F33})$$

$$= \int_{\Omega} \underbrace{\psi^{\epsilon_v} (-1)}_{J_{f0}^{\epsilon_v \epsilon_v}} \psi^{\epsilon_v} d\Omega \quad (\text{F34})$$

934

Appendix G Fault Formulation

For the example of combining a standard PyLith fault with a poroelastic domain we follow (Aagaard, Knepley, Williams, & Walker, 2022) and define a fault as a boundary condition for the mechanics problem prescribing the jump in the displacement field across the fault,

$$\vec{u}^+ - \vec{u}^- - \vec{d}(\vec{x}, t) = \vec{0} \text{ on } \Gamma_f, \quad (\text{G1})$$

where Γ_f is the domain of the boundary on the fault, \vec{u}^+ is the displacement vector on the "positive" side of the fault, \vec{u}^- is the displacement vector on the "negative" side of the fault. For this example, we neglect the inertial term ($\rho\dot{\vec{v}} \approx \vec{0}$). We place all of the terms in the elasticity equation on the left hand side, consistent with implicit time stepping. Our equation of the conservation of momentum on the fault interface reduces to

$$\int_{\Gamma_{f+}} \boldsymbol{\sigma} \cdot \vec{n} + \vec{\lambda} d\Gamma + \int_{\Gamma_{f-}} \boldsymbol{\sigma} \cdot \vec{n} - \vec{\lambda} d\Gamma = 0. \quad (\text{G2})$$

We enforce this equation on each portion of the fault interface along with our prescribed slip constraint, which leads to

$$\boldsymbol{\sigma} \cdot \vec{n} + \vec{\lambda} = \vec{0} \text{ on } \Gamma_{f+}, \quad (\text{G3})$$

$$\boldsymbol{\sigma} \cdot \vec{n} - \vec{\lambda} = \vec{0} \text{ on } \Gamma_{f-}, \quad (\text{G4})$$

$$\vec{u}^+ - \vec{u}^- - \vec{d}(\vec{x}, t) = \vec{0}, \quad (\text{G5})$$

Our solution vector is now expanded to include Lagrange multipliers, and the strong form for the system of equations is

$$\vec{s}^T = \left(\vec{u} \quad p \quad \epsilon_v \quad \vec{\lambda} \right)^T, \quad (\text{G6})$$

$$\vec{f}(\vec{x}, t) + \nabla \cdot \boldsymbol{\sigma}(\vec{u}, \epsilon_v, p) = \vec{0} \text{ in } \Omega, \quad (\text{G7})$$

$$\dot{\zeta}(\epsilon_v, p) + \nabla \cdot \vec{q}(p) - \gamma(\vec{x}, t) = 0 \text{ in } \Omega, \quad (\text{G8})$$

$$\nabla \cdot \vec{u} - \epsilon_v = 0 \text{ in } \Omega, \quad (\text{G9})$$

$$\boldsymbol{\sigma} \cdot \vec{n} = \vec{\tau}(\vec{x}, t) \text{ on } \Gamma_\tau, \quad (\text{G10})$$

$$\vec{u} = \vec{u}_0(\vec{x}, t) \text{ on } \Gamma_u, \quad (\text{G11})$$

$$\vec{q} \cdot \vec{n} = q_0(\vec{x}, t) \text{ on } \Gamma_q, \quad (\text{G12})$$

$$p = p_0(\vec{x}, t) \text{ on } \Gamma_p, \quad (\text{G13})$$

$$\vec{u}^+ - \vec{u}^- - \vec{d}(\vec{x}, t) = \vec{0} \text{ on } \Gamma_f, \quad (\text{G14})$$

$$\boldsymbol{\sigma} \cdot \vec{n} = -\vec{\lambda}(\vec{x}, t) \text{ on } \Gamma_{f+}, \text{ and} \quad (\text{G15})$$

$$\boldsymbol{\sigma} \cdot \vec{n} = +\vec{\lambda}(\vec{x}, t) \text{ on } \Gamma_{f-}. \quad (\text{G16})$$

We create the weak form by taking the dot product with the trial function $\vec{\psi}_{trial}^u$ or $\vec{\psi}_{trial}^\lambda$ and integrating over the domain. After using the divergence theorem and in-

corporating the Neumann boundary and fault interface conditions, we have

$$\int_{\Omega} \vec{\psi}_{trial}^u \cdot \vec{f}(\vec{x}, t) + \nabla \vec{\psi}_{trial}^u : -\boldsymbol{\sigma}(\vec{u}) d\Omega + \int_{\Gamma_{\tau}} \vec{\psi}_{trial}^u \cdot \vec{\tau}(\vec{x}, t) d\Gamma, \\ + \int_{\Gamma_f} \vec{\psi}_{trial}^{u+} \cdot (-\vec{\lambda}(\vec{x}, t)) + \vec{\psi}_{trial}^{u-} \cdot (+\vec{\lambda}(\vec{x}, t)) d\Gamma = 0 \quad (\text{G17})$$

$$\int_{\Omega} \psi_{trial}^p \cdot (\dot{\zeta}(\vec{u}, p_f) - \gamma(\vec{x}, t)) + \nabla \psi_{trial}^p \cdot -\vec{q}(p_f) d\Omega + \int_{\Gamma_q} \psi_{trial}^p \cdot [q_0(\vec{x}, t)] d\Gamma, \quad (\text{G18})$$

$$\int_{\Omega} \psi_{trial}^{\epsilon} \cdot (\nabla \cdot \vec{u} - \epsilon_v) d\Omega. \quad (\text{G19})$$

$$\int_{\Gamma_f} \vec{\psi}_{trial}^{\lambda} \cdot (-\vec{u}^+ + \vec{u}^- + \vec{d}(\vec{x}, t)) d\Gamma = 0. \quad (\text{G20})$$

935 We solve the system of equations using implicit time stepping, making use of residual
936 functions and Jacobians for the left hand side.

937 G1 Residual Equations

We only write the expressions for left hand side equations $F(t, s, \dot{s})$, as in the implicit formulation $G(t, s) = 0$,

$$F^u(t, s, \dot{s}) = \int_{\Omega} \underbrace{\vec{\psi}_{trial}^u \cdot \vec{f}(\vec{x}, t)}_{\vec{f}_0^u} + \nabla \vec{\psi}_{trial}^u : \underbrace{-\boldsymbol{\sigma}(\vec{u})}_{\mathbf{f}_1^u} d\Omega + \int_{\Gamma_{\tau}} \underbrace{\vec{\psi}_{trial}^u \cdot \vec{\tau}(\vec{x}, t)}_{\vec{f}_0^u} d\Gamma \\ + \int_{\Gamma_f} \underbrace{\vec{\psi}_{trial}^{u+} \cdot (-\vec{\lambda}(\vec{x}, t))}_{\vec{f}_0^u} + \underbrace{\vec{\psi}_{trial}^{u-} \cdot (+\vec{\lambda}(\vec{x}, t))}_{\vec{f}_0^u} d\Gamma \quad (\text{G21})$$

$$F^p(t, s, \dot{s}) = \int_{\Omega} \underbrace{\psi_{trial}^p (\dot{\zeta}(\vec{u}, p_f) - \gamma(\vec{x}, t))}_{f_0^p} + \nabla \psi_{trial}^p \cdot \underbrace{-\vec{q}(p_f)}_{\mathbf{f}_1^p} d\Omega + \int_{\Gamma_q} \underbrace{\psi_{trial}^p q_0(\vec{x}, t)}_{f_0^p} d\Gamma, \quad (\text{G22})$$

$$F^{\epsilon}(t, s, \dot{s}) = \int_{\Omega} \underbrace{\psi^{\epsilon} \cdot (\nabla \cdot \vec{u} - \epsilon_v)}_{f^{\epsilon_0}} d\Omega. \quad (\text{G23})$$

$$F^{\lambda}(t, s, \dot{s}) = \int_{\Gamma_f} \underbrace{\vec{\psi}_{trial}^{\lambda} \cdot (-\vec{u}^+ + \vec{u}^- + \vec{d}(\vec{x}, t))}_{\vec{f}_0^{\lambda}} d\Gamma. \quad (\text{G24})$$

For the sake of brevity we only list the nonzero additional Jacobians relative to those listed in Appendix Appendix F,

$$J_F^{u\lambda} = \frac{\partial F^u}{\partial \lambda} + s_{tshift} \frac{\partial F^u}{\partial \dot{\lambda}} = \int_{\Gamma_f} \underbrace{\psi_{trial i}^{u+} (-\delta_{ij}) \psi_{basis j}^{\lambda}}_{J_{f_0^u}^{u\lambda}} + \underbrace{\psi_{trial i}^{u-} (+\delta_{ij}) \psi_{basis j}^{\lambda}}_{J_{f_0^u}^{u\lambda}} d\Gamma, \\ J_F^{\lambda u} = \frac{\partial F^{\lambda}}{\partial u} + s_{tshift} \frac{\partial F^{\lambda}}{\partial \dot{u}} = \int_{\Gamma_f} \underbrace{\psi_{trial i}^{\lambda} (-\delta_{ij}) \psi_{basis j}^{u+}}_{J_{f_0^{\lambda}}^{\lambda u}} + \underbrace{\psi_{trial i}^{\lambda} (+\delta_{ij}) \psi_{basis j}^{u-}}_{J_{f_0^{\lambda}}^{\lambda u}} d\Gamma, \quad (\text{G25})$$

$$J_F^{\lambda\lambda} = \mathbf{0}.$$